UCLouvain

École polytechnique de Louvain

Multi-scale simulation of granular flows

Author: **Manon WOUTERS**
Supervisors: **Vincent LEGAT, Jonathan LAMBRECHTS**
Readers: **Michel HENRY, Evelyne VAN RUYMBEKE**
Academic year 2021–2022
Master [120] in Electro-mechanical Engineering

Abstract

Granular flows can be solved with numerical simulations. Via the *MigFlow* software, a numerical simulation project, a better understanding of the viscoelastic properties of suspensions can be provided. In the aim of this thesis, we simulated a simple shear in order to analyze the viscosity curve as a function of the compacity. By realizing that *MigFlow* computed wrong results, we worked on the modification of the software to obtain results in agreement with the models of the literature. Moreover, a parametric study was performed to observe the influence of the friction coefficient and the shear rate on the viscosity. The normal forces applied by the grains on the domain boundaries were also discussed. Furthermore, a frequency analysis was performed to evaluate the stress response of the flow to a sinusoidal deformation. These last results were compared to scientific literature data to assess their consistency with the reality. Finally, the complex shear modulus was studied and confirmed by the literature. We notice that there are still some errors which means that the exact physical properties are not accurately obtained. But in general the results are quite consistent with reality, which is promising for the project.

Acknowledgments

First of all, I would like to thank my supervisors Vincent Legat and Jonathan Lambrechts for their guidance and support throughout this academic year.

Furthermore, I would like to thank Michel Henry for his valuable assistance and time, to guide and advise through the advancement of this thesis.

I thank Evelyne Van Ruymbeke for accepting to read my work.

I would like to express my gratitude to Eléonore Lieffrig, Lara Wautier and Thibault Servais for the time they spent reviewing my work and for their advice.

Finally, I would like to thank my family for their ongoing support and I would like to warmly thank my friends Natale Badibanga, Maxime Spira and Quentin Dessain for their unwavering support throughout this rough year.

Contents

Introduction

Rheology is a branch of physics which studies the response of matter when it is subjected to a force and it includes viscosity, elasticity and viscoelasticity. Rheology has many applications in various domains such as medicine with the analysis of the blood cell deformability in order to predict blood diseases [1], geophysics with the study of soils in order to prevent catastrophic landslides [2], food industry with the quality control of certain products [3] or mechanical fabrication with the optimisation of parameters to extrude a material[4].

Depending on the type of material, the response to the force is different. Liquids and gases flow while solids deform, expecting them to return to their original positions once the force is removed[5]. Elasticity is the ability of a material to store and release energy after experiencing a deformation whereas viscosity is its capacity to disperse energy. Viscoelasticity is used to define materials which have both viscous and elastic properties.

Considering the fluids, two types of flow can be defined. On the one hand, there are Newtonian fluids for which the shear stress is proportional to the shear rate and this ratio is known as the dynamic viscosity. On the other hand, there are non-Newtonian fluids, such as suspensions, for which this property is no longer valid. Indeed for this kind of fluid, the viscosity does not depend only on the flow condition. It must also take into account the kinematic history of the fluid [6].

In this thesis, we will focus mainly on non-Newtonian fluids and we will investigate the viscoelastic properties of suspensions. We will use numerical simulations to model this. To do so, we will use an open source software, *MigFlow*[7] (Model for Immersed Granular Flows) which results from a collaboration between the Université Catholique de Louvain and the Université de Montpellier. The program is used to simulate immersed granular flows in different domains such as engineering, geology, chemistry, pharmacology, agriculture. Therefore be able to understand some processes and natural phenomena. We will also verify that the program correctly reflects the theory.

The first chapter is a state of the art on viscosity. The different instruments for viscosity measurements are presented as well as the models proposed by different scientists for viscosity. The approach to obtain the equations of motion for suspensions is described. In the second chapter, we modelise a shear to better understand viscosity properties. In order to achieve this, we explain the working principle of *MigFlow* and present the equations that it uses. The problem domain is exposed along with the method to generate the mesh and the grains. Then, we present the necessary modifications that we have implemented in the code to meet the expectations of the literature. After validating our

model in the previous chapter, we perform a parametric analysis in chapter 3. We study both the influence of the coefficient of friction and the shear rate. Then, we discuss about the normal forces due to the grains. Finally, the last chapter deals with a frequency analysis on the shear. First, the theoretical behavior of this type of materials in response to this type of shear is presented as well as the influence of the frequency. Second, we compare it with our results to see if our model has the expected behavior.

Chapter 1

Viscosity in suspensions

Viscosity is one of the main parameters studied in rheology. The viscosity of a fluid is defined as a measure of its resistance to the deformation caused by an applied force. In this chapter, we will start by describing the different measuring instruments for viscosity. Then, we present the different studies that have been done in order to obtain the viscosity of water, which is necessary to measure the viscosity of a fluid more simply. Afterwards, we describe the different models of the literature for the calculation of viscosity. And we finish by explaining the approach to obtain the equations of motion of a suspension.

1.1 Measurement of viscosity

The methods to measure viscosity are quite numerous and the choice of the best instrument adapted to a situation is complex.

They are mainly divided into four categories. The first one are the rotating viscometers. There is the Brookfield viscometer which consists of a rod rotated by a motor through a calibrated spring, immersed in the fluid. Given a spring deformation, the corresponding viscosity can be found on tables provided by the manufacturer [8]. There is also the Couette viscometer. It is composed of two concentric cylinders, one is rotated by a motor, the other one is fixed and there is a fluid between the two. The torque needed to prevent the rotation of the fixed cylinder is measured, giving us the viscosity [9].

Then, there is the capillary viscometer made up of a small diameter capillary in which a liquid is forced to flow. The capillary is located between two reservoirs. Based on the Hagen-Poiseuille equation, the viscosity of a fluid is proportional to the pressure drop of the flow at an imposed velocity in a capillary [10].

Another one that is widely used is the oscillating viscometer. It consists of a body that is suspended from a support making a pendulum. If the body is made to oscillate in vacuum it will oscillate indefinitely. Whereas, if it is made to oscillate in a fluid, it will gradually decrease until it will stop. As it is due to the viscosity of the liquid, it allows us to calculate it[11].

The last category contains special purpose viscometers. One of them is called a penetrometer. It consists of making an object penetrate the product either by subjecting it

to a force or to its own weight. Then, one measures either the evolution of the force of reaction or the time that the object took to travel a certain distance. These values give us the possibility to compute the viscosity [12].

Determining the viscosity of a liquid is a complex, and time-consuming task. However there are very accurate laboratory instruments to measure the viscosity relative to the viscosity of an already known substance and the job is much simpler. The viscosity of water was considered to be the primary standard of viscosity as it is a easily available. The international agreement is to take the absolute viscosity of water at 20°C and atmospheric pressure (101325[Pa]). Therefore, there have been lots of discussion about it. For many years, the standard value was taken at 1.005 [mPas]. In 1952, Swindells et al. [13] decided to start the project of determining this value more precisely. They used a capillary viscometer to perform their experiment and they found a value of 1.0019 [mPas] with an accuracy of ±0.0003[mPas]. Then, several persons tried to obtain a value for the viscosity of water with different methods. Among them, there was Roscoe et al. [14] in 1958, Kestin et al. [15] in 1981, and Berstad et al. [16] in 1988. All the values and their relative uncertainties are listed in Table 1.1.

Year	Author	Viscosity at 20°C [mPas]	Relative uncertainty
1952	Swindells et al.	1.0019	$\pm 3e-4$
1958	Roscoe et al.	1.0025	$\pm 5e-4$
1981	Kestin et al.	1.00249	$\pm 2.6e-3$
1988	Berstad et al.	1.00035	$\pm 5e-4$

Table 1.1: Viscosity values of water.

The International Association for the Properties of Water and Steam (IAPWS) released a very precise but also very complicated formula to calculate the viscosity of ordinary water in 2008 based on former work [17]. Then, in 2011, it published a supplementary release for the properties of water at 0.1[MPa]. It contains a formula which approximates closely the one of 2008, and is way easier to use:

$$\eta_{water,20°C}[MPas] = 280.68T_*^{-1.9} + 511.45T_*^{-7.7} + 61.131T_*^{-19.6} + 0.45903T_*^{-40} \quad (1.1)$$

where $T_*[K] = \frac{T}{300}$. This formula is applicable from 253.15[K] to 383.15 [K]. It gives the value of the viscosity of water at 20°C:

$$\eta_{water,20°C} = 1.0016[\text{mPas}] \quad (1.2)$$

This value has an uncertainty of 0.17% [18]. And it is consistent with the ISO/TR 3666:1998 standard reference value.

1.2 Definition and model for viscosity

Mathematically, the viscosity of a fluid is proportional to the shear stress σ_{xy} and the shear rate $\dot{\gamma} = du/dy$, with u, the velocity

$$\eta_{liq} = \frac{\sigma_{xy}}{\dot{\gamma}} \quad (1.3)$$

The viscosity of a suspension depends on the compacity, i.e. the volume fraction of the particles, the type of liquid and particularly its viscosity, the type of particles and the shear rate.

Many scientists have been interested in calculating this effective viscosity. Einstein is the pioneer. Indeed, all others based their work on it afterwards. Einstein studied particles as rigid, devoid of any attractive forces and uncharged. The interactions between particles is not taken into account and therefore the particles are only set in motion by the fluid. As we are in a shear, the upper part of our domain is in motion while the lower part is static. Therefore, the velocity on the top of the particle is higher than the one on the bottom, resulting in a rotation of the particle as it can be seen on illustration 1.1.

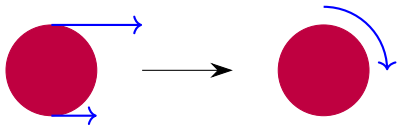

Figure 1.1: Shear effect on a particle.

In 1906 [19], he found the effective viscosity to be linearly related to the particle concentration

$$\frac{\eta_{eff}}{\eta_{liq}} = 1 + c \tag{1.4}$$

with c, the compacity.

But then he was informed by Bacelin, who was doing research on viscosity under Perrin's direction, that he had found values for the viscosity higher than those obtained with the formula of Einstein. Therefore, he asked Hopf to check his work, and he found an error. Einstein then corrected his mistake in 1911 [20]

$$\frac{\eta_{eff}}{\eta_{liq}} = 1 + Bc \tag{1.5}$$

with B, the Einstein coefficient known as the intrinsic viscosity which is 2.5 for a suspension of hard spheres. Since the particles interactions are not considered, this equation is valid only for very low concentration (c<0.01).

Batchelor [21] modified this equation by adding the contributions of Brownian motion of particles to the bulk stress. This is done by considering an expression constructed in terms of hydrodynamic interactions between the particles

$$\frac{\eta_{eff}}{\eta_{liq}} = 1 + Bc + kc^2 \tag{1.6}$$

with k=6.2 for Brownian suspensions in any flow. This equation is valid for concentration larger than those of Einstein, but they remain very small (c<0.1).

In order to take into account bigger concentration, Krieger and Dougherty [22] proposed a semi-empirical expression

$$\frac{\eta_{eff}}{\eta_{liq}} = (1 - \frac{c}{c_{max}})^{-Bc_{max}} \tag{1.7}$$

with c_{max}, the maximum concentration, which appears when the fluid is no longer sufficient to make the particles move. This value is still in discussion and its determination is an undetermined problem. Therefore, it is used as a parameter that can be adjusted in order to fit the experimental data. This value depends on the size of the particles and their interactions.

1.3 Equation of motion for suspensions

To define the motion for a system of fluidized particles, the Navier-Stokes equations are used for the fluid phase and the Newtonian equations for the particles. However, the difficulty lies in the fact that when many particles are close to each other, a direct solution is hard to find and simplifying solutions must be found. Several attempts are found in the literature and a closer look at the one made by Anderson and Jackson [23] is taken.

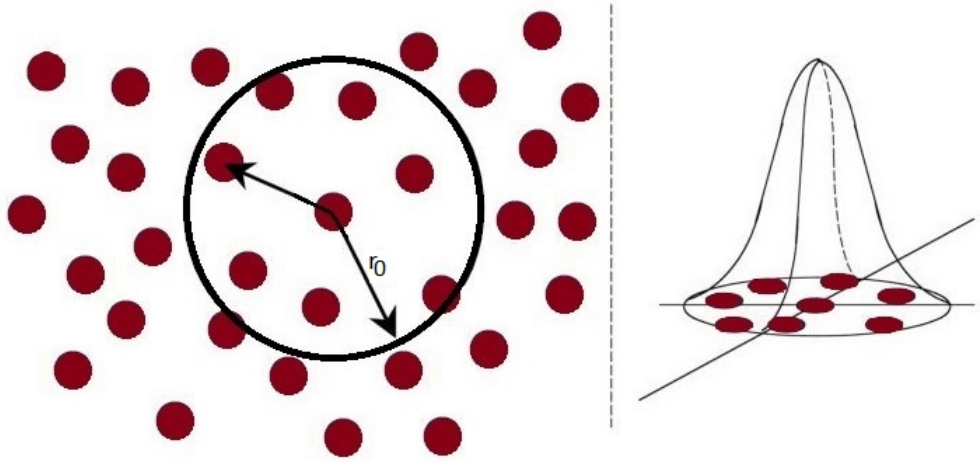

Figure 1.2: Weighting function [24]

The method that they apply to simplify this is to replace mechanical variables by local mean variables, which is done by taking the average of the points variables over large regions compared to the spacing of the particles but small compared to the complete system. In order to do so, a weighting function $g(r)$ (for $r > 0$) is defined and can be seen in figure 1.2. $g(r)$ is bigger than 0 and decreases monotically when r increases. There are derivatives of all orders for each value of r.

$\int_{V_\infty} g^{(n)}(r)dV$ exists for all values of n, with r the distance from a point in a three-dimensional space and V_∞ indicates that the integral is taken over the whole space. As $g(r)$ is normalized,

$$\int_{V_\infty} g(r)dV = 4\pi \int_0^\infty g(r)r^2 dr = 1 \tag{1.8}$$

These properties assure that common operations of the vector calculus and other mathematical operations can be performed. The radius of the weighting function r_0 is defined

by

$$4\pi \int_0^{r_0} g(r) r^2 dr = 4\pi \int_{r_0}^{\infty} g(r) r^2 dr = 0.5 \tag{1.9}$$

The local mean voidage $\boldsymbol{\epsilon}$ (or porosity), at a point $\mathbf{x}$ and time t is defined by

$$\boldsymbol{\epsilon}(\mathbf{x}, t) = \int_{V_{f\infty}(t)} g(|\mathbf{x} - \mathbf{y}|) dV_y \tag{1.10}$$

where $V_{f\infty}(t)$ indicates that the integral is taken over all points $\mathbf{y}$ occupied by fluid at time t and dV_y is an element of volume in the neighborhood of point $\mathbf{y}$.

The local mean particle density (or number of particles per unit volume) $n(\mathbf{x}, t)$ is defined by

$$\nu n(\mathbf{x}, t) = 1 - \boldsymbol{\epsilon}(\mathbf{x}, t) = 1 - \int_{V_{f\infty}(t)} g(|\mathbf{x}-\mathbf{y}|) dV_y = \int_{V_\infty} g(|\mathbf{x}-\mathbf{y}|) dV_y - \int_{V_{f\infty}(t)} g(|\mathbf{x}-\mathbf{y}|) dV_y \tag{1.11}$$

with ν, the volume of one particle.

The set of all points occupied by solid matter at time t is $V_{s\infty}(t)$ and is defined as $V_{s\infty}(t) = V_\infty - V_{f\infty}(t)$. Therefore,

$$\nu n(\mathbf{x}, t) = \int_{V_{s\infty}(t)} g(|\mathbf{x} - \mathbf{y}|) dV_y \tag{1.12}$$

The point value of a variable can be defined as the sum of its local mean value and a fluctuation about this value

$$u'(\mathbf{x}, t) = u(\mathbf{x}, t) + u''(\mathbf{x}, t) \tag{1.13}$$

This is illustrated in figure 1.3

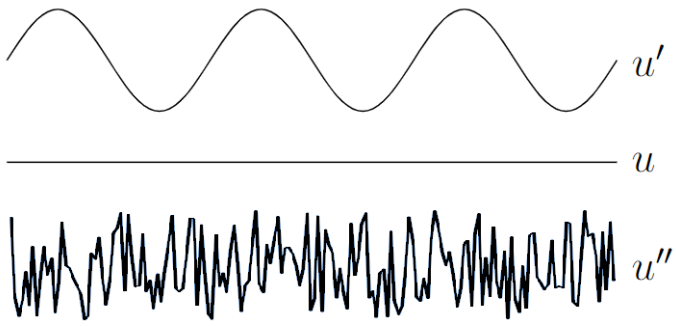

Figure 1.3: Point value decomposition.

Taking $a'(\mathbf{x}, t)$ as any point property of the fluid phase, its local mean value a is defined by

$$\boldsymbol{\epsilon}(\mathbf{x}, t) a(\mathbf{x}, t) = \int_{V_{f\infty}(t)} a(\mathbf{y}, t) g(|\mathbf{x} - \mathbf{y}|) dV_y \approx a(\mathbf{x}, t) \int_{V_{f\infty}(t)} g(|\mathbf{x} - \mathbf{y}|) dV_y \tag{1.14}$$

knowing that the spatial variation of g is fast in comparison to that of the local mean variables and therefore their values hardly change over distances comparable with r_0.

And similarly, taking $b'(\mathbf{x},t)$ as any properties of the solid phase, its local mean value b is defined by

$$\begin{aligned}[1-\boldsymbol{\epsilon}(\mathbf{x},t)]b(\mathbf{x},t) = \nu n(\mathbf{x},t)b(\mathbf{x},t) &= \int_{V_{s\infty}(t)} b'(\mathbf{y},t)g(|\mathbf{x}-\mathbf{y}|)dV_y \\ &\approx \sum_{p\infty} g(|\mathbf{x}-\mathbf{x}_p|)\int_{v_p(t)} b'(\mathbf{y},t)dV_y = \sum_{p\infty}\nu b_p(t)g(|\mathbf{x}-\mathbf{x}_p|)\end{aligned} \tag{1.15}$$

with $v_p(t)$ indicating that the integral is taken over the interior of particle p at time t, $\mathbf{x}_p$ the position of the center of mass of particle p at time t, $b_p(t)$ the average value of b' taken inside the particle p and $\sum_{p\infty}$ using to sum over all particles of the system. The approximation is made knowing that g doesn't vary a lot inside a particle as we can see in figure 1.2.

Therefore it can be simplified as

$$n(\mathbf{x},t)b(\mathbf{x},t) = \sum_{p\infty} b_p(t)g(|\mathbf{x}-\mathbf{x}_p|) \tag{1.16}$$

And in the particular case of $b'=1$,

$$n(\mathbf{x},t) = \sum_{p\infty} g(|\mathbf{x}-\mathbf{x}_p|) \tag{1.17}$$

From now on, the independent variables on which properties depend will not be explicitly noted. For example, $\boldsymbol{\epsilon}(\mathbf{x},t)$ becomes $\boldsymbol{\epsilon}(\mathbf{x})$.

The relation between the spatial and temporal derivatives of the local mean variables and the corresponding derivatives of their associated point variables must be considered to construct the equations of motion.

For the fluid phase, the following relations are obtained

$$\int_{V_{f\infty}(t)} g(|\mathbf{x}-\mathbf{y}|)\frac{\partial a'(\mathbf{y})}{\partial y_k}dV_y = \frac{\partial}{\partial x_k}[\boldsymbol{\epsilon}(\mathbf{x})a(\mathbf{x})] - \sum_{p\infty}\int_{s_p(t)} n_k a'(\mathbf{y})g(|\mathbf{x}-\mathbf{y}|)dS_y \tag{1.18}$$

$$\int_{V_{f\infty}(t)} g(|\mathbf{x}-\mathbf{y}|)\frac{\partial a'(\mathbf{y})}{\partial t}dV_y = \frac{\partial}{\partial t}[\boldsymbol{\epsilon}(\mathbf{x})a(\mathbf{x})] + \sum_{p\infty}\int_{s_p(t)} a'(\mathbf{y})n_k v'_k(\mathbf{y})g(|\mathbf{x}-\mathbf{y}|)dS_y \tag{1.19}$$

with n_k, the outward normal to the fluid at points on its boundary, $s_p(t)$, the surface of a particle and $v'_k(\mathbf{y})$, the velocity of solid matter at a point $\mathbf{y}$ lying in particle p at time t.

Then for the solid phase,

$$\sum_{p\infty}\int_{v_p(t)} g(|\mathbf{x}-\mathbf{y}|)\frac{\partial b'(\mathbf{y})}{\partial y_k}dV_y = \frac{\partial}{\partial x_k}[(1-\boldsymbol{\epsilon}(\mathbf{x}))b(\mathbf{x})] + \sum_{p\infty}\int_{s_p(t)} n_k b'(\mathbf{y})g(|\mathbf{x}-\mathbf{y}|)dS_y \tag{1.20}$$

$$\sum_{p\infty}\int_{v_p(t)} g(|\mathbf{x}-\mathbf{y}|)\frac{\partial b'(\mathbf{y})}{\partial t}dV_y = \frac{\partial}{\partial t}[(1-\boldsymbol{\epsilon}(\mathbf{x}))b(\mathbf{x})] - \sum_{p\infty}\int_{s_p(t)} b'(\mathbf{y})n_k v'_k(\mathbf{y})g(|\mathbf{x}-\mathbf{y}|)dS_y \tag{1.21}$$

Using all these equations, they started from the Navier-Stokes equation to determine the equation of motion for the fluid

$$\rho_f \left[\frac{\partial u_i'}{\partial t} + \frac{\partial}{\partial y_k}(u_i' u_k') \right] = \frac{\partial E_{ik}'}{\partial y_k} + \rho_f g_i \tag{1.22}$$

with E_{ik}', the point value of the fluid stress tensor and g_i, a vector pointing vertically downward and equal in magnitude to the gravitational force per unit mass.

Taking local averages on both side,

$$\begin{aligned} \rho_f \int_{V_{f\infty}(t)} g(|\mathbf{x}-\mathbf{y}|) \left[\frac{\partial u_i'}{\partial t} + \frac{\partial}{\partial y_k}(u_i' u_k') \right] dV_y = & \int_{V_{f\infty}(t)} g(|\mathbf{x}-\mathbf{y}|) \frac{\partial E_{ik}'}{\partial y_k} dV_y \\ & + \rho_f g_i \int_{V_{f\infty}(t)} g(|\mathbf{x}-\mathbf{y}|) dV_y \end{aligned} \tag{1.23}$$

The left part of equation 1.23 is firstly written in terms of local mean variables thanks to equations 1.18 and 1.19 and to the fact that the velocities of the fluid and the particle are equal at all points on the surface of a particle. Then, using the definition of a point value, equation 1.14 and the fact that local mean values of fluctuations u_i'' and u_k'' are negligible, this part of the equation can be rewritten

$$\begin{aligned} \rho_f \int_{V_{f\infty}(t)} g(|\mathbf{x}-\mathbf{y}|) \left[\frac{\partial u_i'}{\partial t} + \frac{\partial}{\partial y_k}(u_i' u_k') \right] dV_y = & \rho_f \left[\frac{\partial}{\partial t}(\boldsymbol{\epsilon}(\mathbf{x}) u_i(\mathbf{x})) + \frac{\partial}{\partial x_k}(\boldsymbol{\epsilon}(\mathbf{x}) u_i(\mathbf{x}) u_k(\mathbf{x})) \right] \\ & + \frac{\partial R_{ik}}{\partial x_k} \end{aligned} \tag{1.24}$$

with

$$R_{ik} = \rho_f \int_{V_{f\infty}(t)} u_i''(\mathbf{y}) u_k''(\mathbf{y}) g(|\mathbf{x}-\mathbf{y}|) dV_y \tag{1.25}$$

The second term on the right-hand side of equation 1.23 can be easily simplified to $\boldsymbol{\epsilon}(\mathbf{x})\rho_f g_i$ with equation 1.10. For the first term, they used equation 1.18, the Gauss's theorem and the equation $\partial g(|\mathbf{x}-\mathbf{y}|)/\partial y_k = -\partial g(|\mathbf{x}-\mathbf{y}|)/\partial x_k$ in order to simplify it. As well as the fact that E_{ik} and $\partial E_{ik}/\partial y_k$ does not vary a lot over distances comparable to r_0, and that $g(|\mathbf{x}-\mathbf{y}|)$ varies little over distances comparable with the particle diameter. The term becomes

$$\int_{V_{f\infty}(t)} g(|\mathbf{x}-\mathbf{y}|) \frac{\partial E_{ik}'}{\partial y_k} dV_y = \boldsymbol{\epsilon}(\mathbf{x}) \frac{\partial E_{ik}(\mathbf{x})}{\partial x_k} - \sum_{p\infty} g(|\mathbf{x}-\mathbf{x}_p|) \int_{s_p(t)} n_k E_{ik}'' dS_y \tag{1.26}$$

Then, equation 1.23 can be rewritten thanks to equations 1.24, 1.25, 1.26 and to the fluid continuity equation $\partial\epsilon/\partial t + \partial(\epsilon u_k)/\partial x_k = 0$,

$$\rho_f \boldsymbol{\epsilon} \left[\frac{\partial u_i}{\partial t} + u_k \frac{\partial u_i}{\partial x_k} \right] = \boldsymbol{\epsilon} \frac{\partial E_{ik}}{\partial x_k} - \frac{\partial R_{ik}}{\partial x_k} + \boldsymbol{\epsilon}\rho_f g_i - \sum_{p\infty} g(|\mathbf{x}-\mathbf{x}_p|) \int_{s_p(t)} n_k E_{ik}'' dS_y \tag{1.27}$$

Using the divergence theorem and the fact that $\partial E_{ik}/\partial x_k$ does not vary a lot over the interior of a particle, the force exerted on a single particle p by the surrounding fluid can be written

$$f_{pi} = \int_{s_p(t)} E'_{ik} n_k dS = \nu \left(\frac{\partial E_{ik}}{\partial d_k} \right)_{x_p} + \int_{s_p(t)} E''_{ik} n_k dS \tag{1.28}$$

And with the help of equation 1.16, 1.17, the fact that $\partial E_{ik}/\partial x_k$ doesn't vary a lot over r_0, the last term of the right-hand side of equation 1.27 becomes

$$\sum_{p\infty} g(|\mathbf{x} - \mathbf{x}_p|) \int_{s_p(t)} n_k E''_{ik} dS_y = n(\mathbf{x}) f_i(\mathbf{x}) - [1 - \boldsymbol{\epsilon}(\mathbf{x})] \left(\frac{\partial E_{ik}}{\partial x_k} \right)_x \tag{1.29}$$

And finally, by injecting equation 1.29 into equation 1.27, it gives the final equation of motion for the fluid

$$\boxed{\begin{gathered} \rho_f \boldsymbol{\epsilon} \left[\frac{\partial u_i}{\partial t} + u_k \frac{\partial u_i}{\partial x_k} \right] = \frac{\partial \mathcal{E}_{ik}}{\partial x_k} - n f_i + \boldsymbol{\epsilon} \rho_f g_i \\ \text{with} \\ \mathcal{E}_{ik} = E_{ik} - R_{ik} \end{gathered}} \tag{1.30}$$

For the equation of motion of the solid phase, they begin from the equation of motion for the center of a single particle

$$\nu \rho_s \frac{\partial v_{pi}}{\partial t} = f_{pi} + \nu \rho_s g_i + \phi_{pi} \tag{1.31}$$

with v_{pi}, the i-th component of the velocity of the center of mass, f_{pi}, the force exerted by the surrounding fluid on the particle and ϕ_{pi}, the force experienced by the particle resulting from the interaction with other particles.

Taking the local averages on each side of the equation with the help of equations 1.16, 1.17 and the fact that $n\nu = 1 - \boldsymbol{\epsilon}$,

$$\nu \rho_s \sum_{p\infty} g(|\mathbf{x} - \mathbf{x}_p|) \frac{\partial v_{pi}}{\partial t} = n(\mathbf{x}) f_i(\mathbf{x}) + (1 - \boldsymbol{\epsilon}(\mathbf{x})) \rho_s g_i + n(\mathbf{x}) \phi_i(\mathbf{x}) \tag{1.32}$$

with f_i, the local mean fluid-particle interaction force, and ϕ_i the local mean particle-particle interaction force.

Then, the left-hand side of the equation can be defined as

$$\nu \rho_s \sum_{p\infty} \frac{\partial v_{pi}}{\partial t} g(|\mathbf{x} - \mathbf{x}_p|) = \nu \rho_s \frac{\partial}{\partial t} [n(\mathbf{x}) v_i(\mathbf{x})] + \nu \rho_s \frac{\partial}{\partial x_k} \sum_{p\infty} v_{pi} v_{pk} g(|\mathbf{x} - \mathbf{x}_p|) \tag{1.33}$$

with v_i, the local mean particle velocity.

The second term on the right of equation 1.33 is simplified with the help of equation 1.14, the definition of a point value and the fact that local mean values of fluctuations v''_{pi} and v''_{pk} are negligible. Finally, equation 1.32 can be rewritten in order to obtain the final equation for the motion of the solid phase

$$\boxed{\begin{gathered}\rho_s(1-\boldsymbol{\epsilon})\left[\frac{\partial v_i}{\partial t}+v_k\frac{\partial v_i}{\partial x_k}\right]=nf_i+(1-\boldsymbol{\epsilon})\rho_s g_i+n\phi_i-\frac{\partial S_{ik}}{\partial x_k}\\ \text{with}\\ S_{ik}(\mathbf{x})=\nu\rho_s\sum_{p\infty}v''_{pi}v''_{pk}g(|\mathbf{x}-\mathbf{x}_p|)\end{gathered}} \tag{1.34}$$

Comparing equations 1.30 and 1.34, it is easy to notice that the fluid particle interaction appears in the same form but with different signs, meaning that the third law of Newton is satisfied.

In order to have the state of motion of the system determined, it is necessary to know the dependence of $\mathcal{E}_{ik}, \phi_i, S_{ik}, f_i$ on the porosity, the local mean velocities and the pressure as well as the dependence of E'_{ik} on the fluid pressure and velocity.

Firstly, they look at the direct interaction force between the particles $n\phi_i$, which they expressed as the divergence of a stress tensor $\partial E^s_{ik}/\partial x_k$. This stress tensor includes an isotropic term depending on the porosity and representing the elastic resistance of the particle assembly to compression, as well as terms related to the rate of strain tensor and representing the fluid-like behavior of the assembly. The "Reynolds stress" term $\partial S_{ik}/\partial x_k$ is integrated in the formula

$$n\phi_i-\frac{\partial S_{ik}}{\partial x_k}=\frac{\partial E^s_{ik}}{\partial x_k}-\frac{\partial S_{ik}}{\partial x_k}=\frac{\partial \mathcal{E}^s_{ik}}{\partial x_k} \tag{1.35}$$

Considering that the form of $\mathcal{E}^s_{ik}$ is similar to the stress tensor of a Newtonian fluid, it can be written

$$\mathcal{E}^s_{ik}=-p^s(\boldsymbol{\epsilon})\delta_{ik}+\lambda^s(\boldsymbol{\epsilon})\frac{\partial v_m}{\partial x_m}\delta_{ik}-\mu^s(\boldsymbol{\epsilon})\left[\frac{\partial v_i}{\partial x_k}+\frac{\partial v_k}{\partial x_i}-\frac{2}{3}\delta_{ik}\frac{\partial v_m}{\partial x_m}\right] \tag{1.36}$$

with δ_{ik}, the Kronecker delta, $p^s(\boldsymbol{\epsilon})$, the interparticle pressure, λ^s and μ^s, the effective bulk and shear viscosities for the particle assembly.

Equation 1.34 can be rewritten with equation 1.35

$$\rho_s(1-\boldsymbol{\epsilon})\left[\frac{\partial v_i}{\partial t}+v_k\frac{\partial v_i}{\partial x_k}\right]=\frac{\partial \mathcal{E}^s_{ik}}{\partial x_k}+nf_i+(1-\boldsymbol{\epsilon})\rho_s g_i \tag{1.37}$$

Then, the terms E_{ik} and R_{ik} need to be evaluated. They are found in the term $\partial \mathcal{E}_{ik}/\partial x_k$, which has a form analogous to equation 1.36

$$\mathcal{E}_{ik}=-p\delta_{ik}+\lambda(\boldsymbol{\epsilon})\frac{\partial v_m}{\partial x_m}\delta_{ik}-\mu(\boldsymbol{\epsilon})\left[\frac{\partial v_i}{\partial x_k}+\frac{\partial v_k}{\partial x_i}-\frac{2}{3}\delta_{ik}\frac{\partial v_m}{\partial x_m}\right] \tag{1.38}$$

with p, the local mean fluid pressure and λ and μ, the effective bulk and shear viscosities.

Finally, there is the local mean value of the force per particle which results from the interaction with the fluid f_i. A form is suggested

$$f_i = \alpha(\boldsymbol{\epsilon})(u_i - v_i)h(|u_i - v_i|) + C(\boldsymbol{\epsilon})\nu\rho_f \frac{d}{dt}(u_i - v_i) \tag{1.39}$$

with the first term representing the drag force in the direction of the relative velocity $(u_i - v_i)$ and the second term representing a virtual mass force proportional to the mass of fluid displaced by a particle.

Then, approaching the problem by considering a single particle in a fluid, the total force applied on the particle in the upward vertical direction is

$$f = f_d(u) - \nu\rho_s g - \nu\frac{dp}{dx} \tag{1.40}$$

with the pressure gradient given by $dp/dx = -\rho_f g$, for flow with parallel streamlines as seen in illustration 1.4 on the left and by $dp/dx = -\rho_f g - \rho_f u du/dx$, for flow with diverging streamlines as seen on the right.

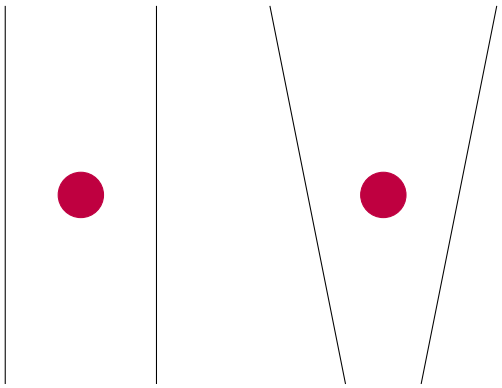

Figure 1.4: Parallel streamlines flow (left), diverging streamlines flow (right).

The first term in equation 1.40 is $f_d(u)$, the drag force. The second term is the buoyancy force and the third terms represent the reaction on the particle of large scale pressure gradients in the fluid. The first and third term together represents the complete fluid-particle interaction force.

Afterwards, the assembly of particles is considered. The force exerted on a single particle induced by the fluid is

$$f_{pi} = \int_{s_p} E'_{ik} n_k dS \tag{1.41}$$

They wanted to decompose this term into two components of the fluid stress tensor, one at a large scale compared with the particle spacing and the other one representing detailed variations, therefore E'_{ik} is rewritten as $E_{ik} + E''_{ik}$, its point value definition. Including the "Reynolds stresses" R_{ik}, it becomes $E'_{ik} = \mathcal{E}_{ik} - \mathcal{D}_{ik}$. Then, using Gauss's theorem and the fact that $\partial\mathcal{E}_{ik}/\partial x_k$ varies little over the interior of a particle,

$$f_{pi} = \int_{s_p} \frac{\partial \mathcal{E}_{ik}}{\partial x_k} dV + \int_{s_p} \mathcal{D}_{ik} n_k dS = \nu \left(\frac{\partial \mathcal{E}_{ik}}{\partial x_k} \right)_{\mathbf{x}_p} + \overline{f}_{pi} \tag{1.42}$$

The term used in equations 1.30 and 1.37 is nf_i, therefore using equation 1.42,

$$nf_i = \sum_{p\infty} f_{pi} g(|\mathbf{x} - \mathbf{x}_p|) = \nu \left(\frac{\partial \mathcal{E}_{ik}}{\partial x_k} \right)_{\mathbf{x}} \sum_{p\infty} g(|\mathbf{x} - \mathbf{x}_p|) + \sum_{p\infty} \overline{f}_{pi} g(|\mathbf{x} - \mathbf{x}_p|) = n\nu \frac{\partial \mathcal{E}_{ik}}{\partial x_k} + n\overline{f}_i \tag{1.43}$$

with the fact that $\partial \mathcal{E}_{ik}/\partial x_k$ varies little over distances comparable with r_0.

Regarding the discussion on the single particle in a fluid, f_{pi} is comparable to the total interaction force, taking $\mathcal{E}_{ik}$ as a pure pressure gives $\partial \mathcal{E}_{ik}/\partial x_k = -\partial p/\partial x_i$ and $\overline{f}_{pi}$ is analogous to $f_d(u)$. Therefore, the equations are similar and it is $\overline{f}_i$ that should be expressed in the form of equation 1.39,

$$n\overline{f_i} = n\alpha(\boldsymbol{\epsilon})(u_i - v_i)h(|u_i - v_i|) + nC(\boldsymbol{\epsilon})\nu\rho_f \frac{d}{dt}(u_i - v_i) \tag{1.44}$$

Finally, the equations of motion 1.30 and 1.37 become

$$\boxed{\rho_f \boldsymbol{\epsilon} \left[\frac{\partial u_i}{\partial t} + u_k \frac{\partial u_i}{\partial x_k} \right] = \boldsymbol{\epsilon} \frac{\partial \mathcal{E}_{ik}}{\partial x_k} - n\overline{f_i} + \boldsymbol{\epsilon}\rho_f g_i} \tag{1.45}$$

$$\boxed{\rho_s (1 - \boldsymbol{\epsilon}) \left[\frac{\partial v_i}{\partial t} + v_k \frac{\partial v_i}{\partial x_k} \right] = (1 - \boldsymbol{\epsilon}) \frac{\partial \mathcal{E}_{ik}}{\partial x_k} + n\overline{f_i} + (1 - \boldsymbol{\epsilon})\rho_s g_i + \frac{\partial \mathcal{E}^s_{ik}}{\partial x_k}} \tag{1.46}$$

with $\mathcal{E}^s_{ik}$ given by equation 1.36, $\mathcal{E}_{ik}$ given by equation 1.38and $n\overline{f_i}$ given by equation 1.44.

Equations 1.30 and 1.37 can be compared with equations 1.45 and 1.46. Depending on how the interaction between the grains and the fluid is expressed, the multiplication factor of the term $\partial \mathcal{E}_{ik}/\partial x_k$ is different. There is still much discussion about how this interaction is defined because no one has yet agreed on a precise way to express it.

Chapter 2

Modelisation of simple shear

We are going to modelise immersed granular flows subjected to shear. For this, we will use a software called *MigFlow*.

In this chapter, we present the *MigFlow* project and the equations that compose it. Then, the parameters of the simulation will be presented as well as the mesh used to represent the problem and the method for the generation of the grains. Finally, we validate the model to see if it corresponds to the expectations of the literature and we make the necessary modifications in the code to respect them as well as possible.

2.1 MigFlow

MigFlow uses multi-scale representation to solve problems of granular flows. The fluid phase is solved on a large scale with respect to the grain size. Like Anderson and Jackson [23], the fluid properties are computed from the Navier-Stokes equations which are averaged over a local control volume using a weighting function. The control volume is a triangle of our mesh and the weighting variable is the porosity ϕ of the flow. It is solved using a stabilized finite element method.

By posing $\mathbf{u} = \phi\mathbf{w}$ the mean velocity of the fluid and stating that the fluid is incompressible, the conservation laws of the fluid are

$$\rho\left(\frac{\partial \mathbf{u}}{\partial t} + \nabla \cdot \frac{\mathbf{uu}}{\phi}\right) = \nabla \cdot [2\eta\phi\mathbf{d}(\mathbf{u}) - p\mathbf{I}] + \mathbf{f} + \phi\rho\mathbf{g} \tag{2.1}$$

$$\frac{\partial \phi}{\partial t} + \nabla \cdot \mathbf{u} = 0 \tag{2.2}$$

with ρ, the density of the fluid, η, the dynamic viscosity, p, the pressure, $\mathbf{f}$, the fluid-grains interaction force, $\mathbf{g}$, the gravity, $\mathbf{I}$, the identity tensor and $\mathbf{d(u)}$, the rate of the deformation tensor, which is defined as follows

$$\mathbf{d}(\mathbf{u}) \triangleq \frac{1}{2}\left(\frac{\mathbf{u}}{\phi} + \left(\nabla\frac{\mathbf{u}}{\phi}\right)^T\right) \tag{2.3}$$

The advantage of this method is that the mesh does not need to be reconstructed at each grain displacement. Therefore we gain in computational time.

The method used to solve the granular phase considers only the contact forces of the grains. This means that when a grain rotates on itself, the fluid does not see the rotation.

First, the velocity of the grain is computed using Newton's second law of motion

$$\frac{d}{dt}(m_i \mathbf{v}_i) = m_i \mathbf{g} - V_i \nabla p|_{\mathbf{x}_i} - \mathbf{f}_i \tag{2.4}$$

with m_i, the mass, V_i, the volume, $\mathbf{x}_i$, the position and $\mathbf{v}_i$, the velocity of the grain. The last two terms represent the grains-fluid interaction force $\mathbf{f}$.

This velocity does not take into account any contact for the moment, so we have to add the contacts with the other grains and those with the fluid.

For the contacts with the other grains, a method of nonsmooth Contact Dynamics is used (NSCD). It must anticipate all potential contacts between grains in order to prevent interpenetration. A pair of grains is more likely to come into contact if they are closer than a specific distance. This distance is set to a grain radius. It also depends on the solid time step, which is chosen so that the fastest grain does not move more than one radius in one time step. Then, all the contact reactions are calculated in order to verify the contact laws. The contact reaction applied on the grain is the sum of all active contacts applied on the grain during the time step.

The friction between two grains is modelised by the Coulomb law

$$f^T = -\mu f^N \tag{2.5}$$

with f^T, the tangential force, f^N, the normal force and μ, the friction coefficient.

The contacts with boundaries are treated in the same way. So the boundaries are defined as objects of infinite mass at rest.

For the interaction between the fluid and a single grain, there is no expression for the drag force that fits all scenarios. The influence of the surrounding grains on the fluid-grain interaction force must be considered. To do this, the fluid-grain interaction force experienced by a single grain must be multiplied by an independent function of the porosity $g(\phi)$

$$\mathbf{f}_i = g(\phi|_{\mathbf{x}_i}) C_d \pi r_i^2 \frac{\rho}{2} \left\| \mathbf{v}_i - \frac{\mathbf{u}}{\phi}|_{\mathbf{x}_i} \right\| (\mathbf{v}_i - \frac{\mathbf{u}}{\phi}|_{\mathbf{x}_i}) \tag{2.6}$$

with r_i, the grain's radius and C_d, the drag coefficient

$$C_d = \left(0.63 + \frac{4.8}{\sqrt{R_{e_i}}} \right)^2 \tag{2.7}$$

with

$$R_{e_i} = \frac{2r_i\rho\phi|_{\mathbf{x}_i}}{\eta}\left\|\mathbf{v}_i - \frac{\mathbf{u}}{\phi}|_{\mathbf{x}_i}\right\| \tag{2.8}$$

The independent function of the porosity is determined with the coefficient $\beta = 1.8$ in order to fit for low and high Reynolds regimes

$$g(\phi|_{\mathbf{x}_i}) = \phi^{-\beta}|_{\mathbf{x}_i} \tag{2.9}$$

It is important to pay attention to the fluid-grain interaction force $\mathbf{f}_i$ because it represents the coupling between our two phases and therefore it strongly influences the grain velocity. A semi-implicit scheme is used to linearise this term and to predict the grain velocity at the next time step. The formula for the force thus becomes

$$\mathbf{f}_i^{n+1} = \left(\frac{1}{\gamma_i^n} + \frac{\Delta t}{m_i}\right)^{-1}\left[\mathbf{v}_i^n - \frac{\mathbf{u}^{n+1}}{\phi^n}|_{\mathbf{x}_i} + \Delta t\left(\mathbf{g} - \frac{V_i\nabla p^{n+1}|_{\mathbf{x}_i}}{m_i}\right)\right] \tag{2.10}$$

with

$$\gamma_i = g(\phi|_{\mathbf{x}_i})C_d\pi r_i^2\frac{\rho}{2}\left\|\mathbf{v}_i - \frac{\mathbf{u}}{\phi}|_{\mathbf{x}_i}\right\| \tag{2.11}$$

This formulation is used during the implicit Euler time integration of the finite element problem. To do this, the fluid velocity is taken at the center of each grain and then interpolated at the nodes of the fluid as it can be seen on illustration 2.1.

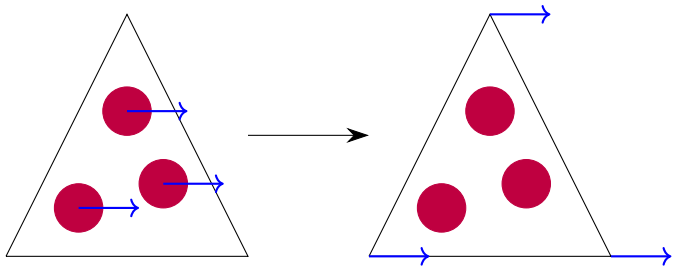

Figure 2.1: Interpolation of fluid velocity.

The benefits of this method are a great time step and good incompressibility. With this solver, the forces between the grains and the stress tensor inside them can be recovered.

2.2 Description of the problem

The domain of our simulation is a rectangle of length five times the height. In order to impose a shear, the top boundary has a velocity of 1 [m/s] and the velocity of the bottom boundary is nul as illustrated in table 2.1. The mean pressure on the domain is fixed to zero.

There are grains randomly distributed throughout the domain and they are dragged with the velocity of the fluid. The compacity varies from 0 to 0.56 [-] (the maximum that

our model is capable of achieving with correct results). In order to simulate an infinite domain, the domain is made periodic, therefore the grains are teleported from the left side to the right side .

On the same table, the different parameters of the simulation are given.

Geometry:

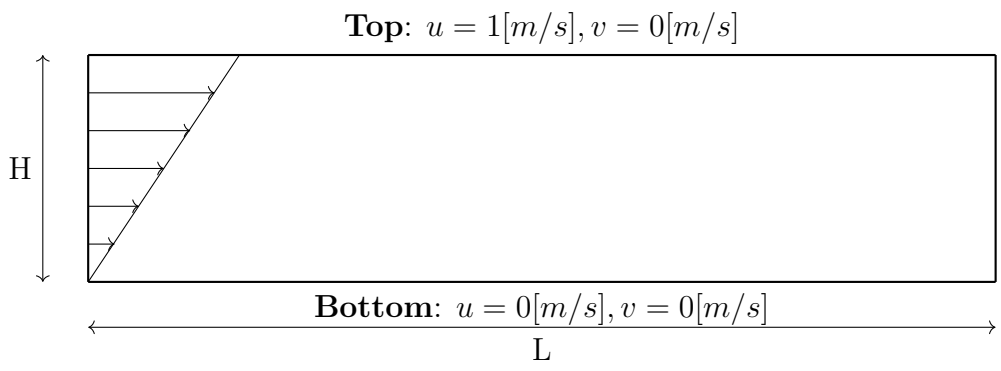

Parameters:

Domain height H = 0.1[m]	Fluid density $\rho = 10^3[kg/m^3]$
Domain length L = 0.5 [m]	Dynamic viscosity $\mu = 1$ [Pas]
Gravity g = 9.81 $[m/s^2]$	Particles density $\rho_p = 10^3[kg/m^3]$
Final time $t_{end} = 2$ [s]	Particles radius $r_p = 10^{-3}$ [m]
Time step $\Delta t = 10^{-3} - 10^{-4}[s]$	Friction coefficient $\mu = 0.5$[-]
Mean pressure p = 0[Pa]	Compacity = 0-0.56 [-]

Table 2.1: Illustration of the problem and boundary conditions.

In order to solve our problem, a mesh is applied on the geometry of the problem. This is done with the GMSH software [25]. It is an open source finite element grid generator. The goal of this software is to be fast, easy to use and light. It uses Computer-Aided Design (CAD) engines to draw the geometry and then the mesh is generated. Figure 2.2 shows the geometry of our problem with the mesh generated by GMSH along with the grains. Here, we take as an example a fluid with a compacity of 0.4 [-].

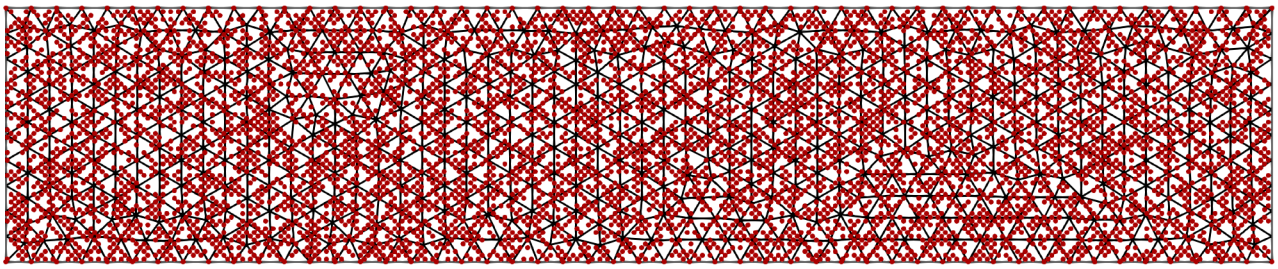

Figure 2.2: Mesh generated by GMSH with grains of compacity 0.4 [-].

The triangles of our mesh are larger than the size of the grains as it can be seen in figure 2.3. Indeed, as we have seen in section 2.1, *MigFlow* uses two different scales to solve the solid and liquid phase equations. The grain scale being smaller than the fluid scale, the mesh is defined to have triangles with sides of approximately 0.01 [m], which is bigger than the radius of grains which is of 10^{-3} [m].

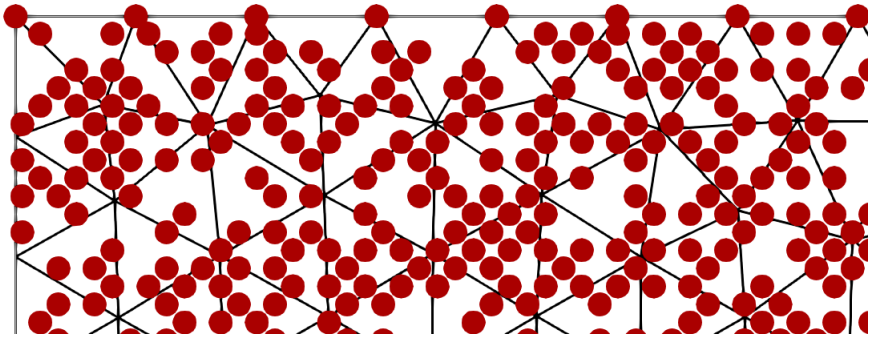

Figure 2.3: Zoom on the problem.

Since we are going to perform the simulation for different compacities, we need to generate the grains in a certain way in order to obtain a specific compacity. Creating the grains in a random way takes a lot of time to compile. Indeed, for each grain generation, the code randomly defines a position then looks if there is already a grain there. If there is no grain, the grain is generated but if there is already one, it starts the process all over again until it finds a place for the grain. Reaching high compacities is therefore very complicated. In order to gain in computational time, we created a matrix containing predefined positions of the grains. We placed the grains in a hexagonal way (see figure 2.4) so that when the matrix is complete, the compacity is of 0.7. Then we make a random mixing of the matrix and the grains are added one by one until the desired compacity is reached.

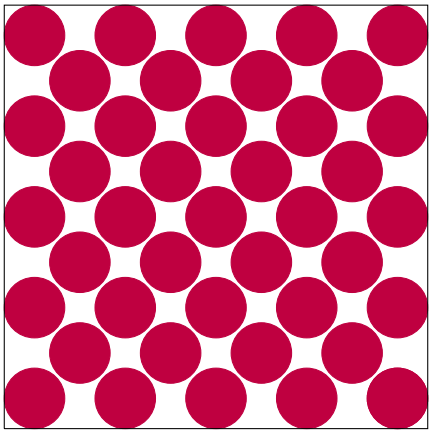

Figure 2.4: Hexagonal arrangement.

2.3 Validation of the model

Going back to our example of a compacity of 0.4 [-], we can verify that the compacity imposed in the code is correct. As we can see in figure 2.5, the mean porosity is of 0.6. Indeed, it is important that the porosity is correctly comprised between 0 and 1 since porosity is our weighting function. The weighting function is used to perform common operations. It allows to give more weight to some elements than to others. Therefore if its value is wrong, it changes all the values obtained from the simulations and all resolutions are thus incorrect.

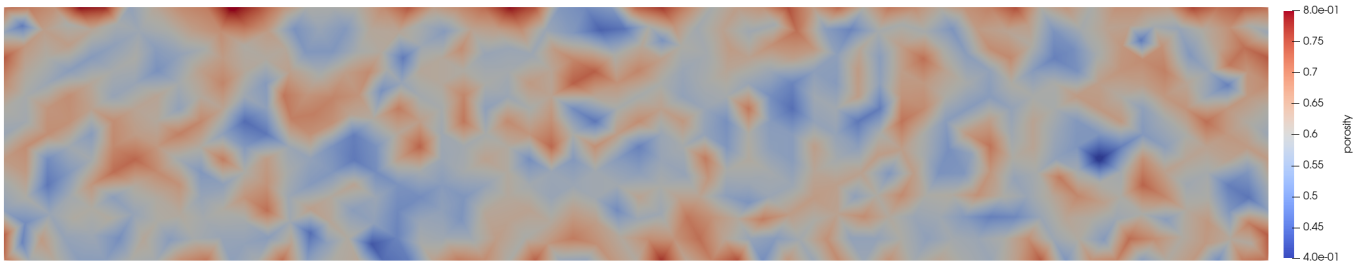

Figure 2.5: Porosity of a simulation of compacity of 0.4 [-].

Then we can validate the fluid velocity. Indeed, we can see on figure 2.6 that the fluid is well established. We have a velocity equal to 1 on the upper boundary as imposed and a zero velocity on the lower boundary. We can observe a Couette flow.

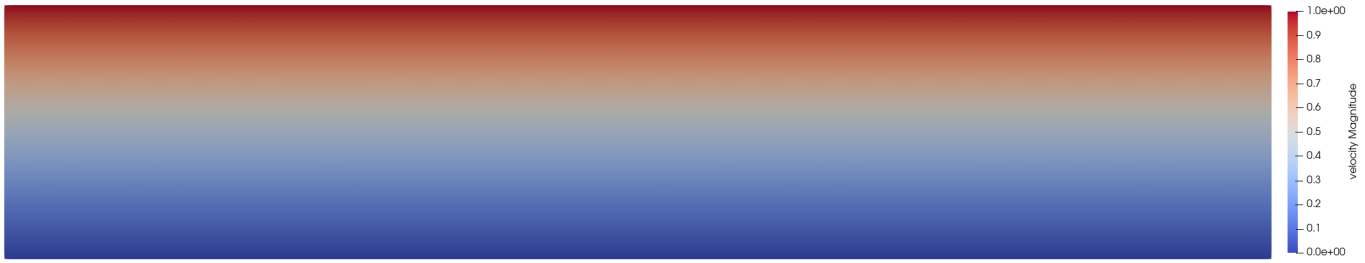

Figure 2.6: Fluid velocity.

As seen in chapter 1, many scientists have proposed a formula to calculate the viscosity of suspensions as a function of the compacity. We made the simulations with *MigFlow* and our results are compared with the laws of Einstein, Batchelor and Krieger, which are summarized in table 2.2.

Einstein	$\frac{\eta_{eff}}{\eta_{liq}} = 1 + 2.5c$
Batchelor	$\frac{\eta_{eff}}{\eta_{liq}} = 1 + 2.5c + 6.2c^2$
Krieger	$\frac{\eta_{eff}}{\eta_{liq}} = (1 - \frac{c}{c_{max}})^{-2.5c_{max}}$

Table 2.2: Summary of used laws, with c, the compacity.

It can be seen in figure 2.7 that the model does not follow the curves of the literature and especially that the viscosity is smaller than 1 for small compacity, which is physically impossible. In the model *MigFlow*, the deformation tensor is multiplied by the porosity in the equation of motion for the fluid (equation 2.1). And as we have seen before with the work of Anderson and Jackson [23] in section 1.3, this term can be expressed with or without the multiplication by the porosity depending on the way the fluid-grain interaction force is defined. Therefore, we have tried to suppress the multiplication by the porosity in the code.

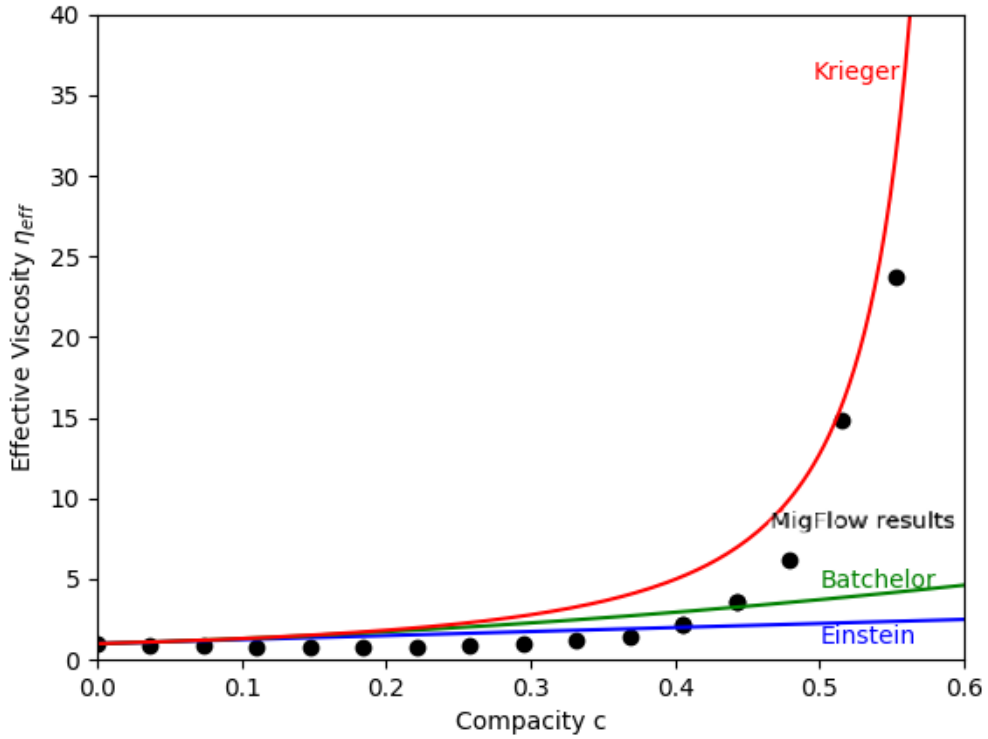

Figure 2.7: Viscosity in function of compacity compared to the literature without any modification in the code.

We can see in figure 2.8 that the viscosity is now always higher than 1. Nevertheless, the curve still does not correspond to the Krieger curve. This is due to the fact that the model does not work at too small scales, it is unable to take into account the interactions present inside a particle. Moreover, as it has already been mentioned, the fluid does not see the rotation of the grains, their influence on the fluid is thus underestimated as the fluid only sees the drag force. To resolve that, we tried to replace what the model does not see by a constitutional law. We chose Batchelor's law as it is of second order. And also because we did not want to take a too complex law so that the collisions between particles are taken into account by our code and not by the constitutive law. The viscosity is therefore multiplied by this law in our code.

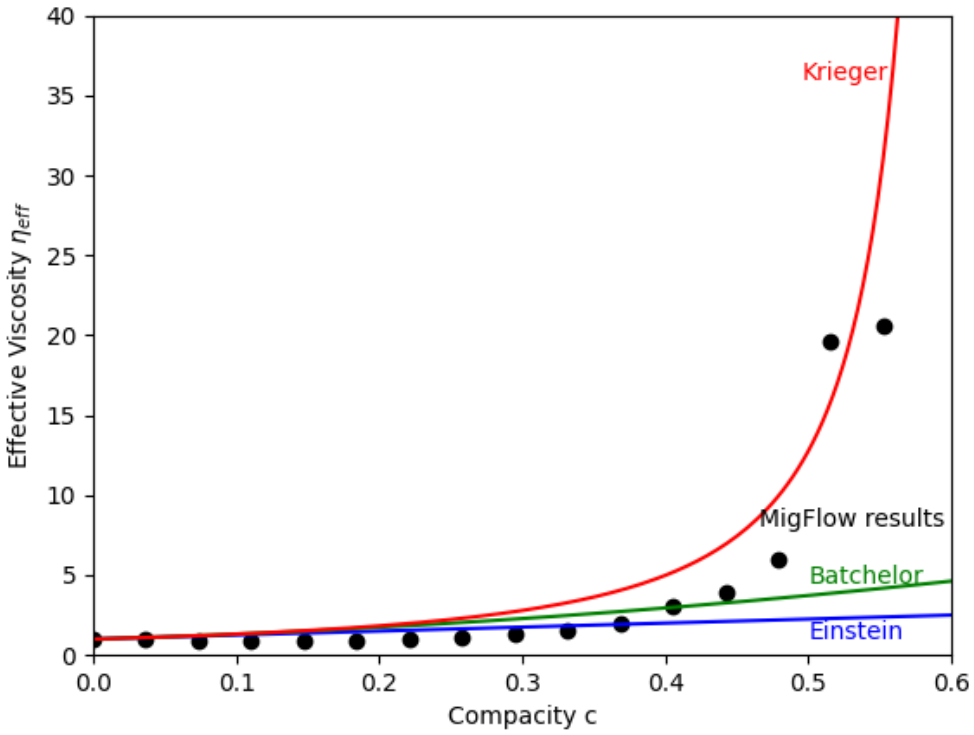

Figure 2.8: Viscosity in function of compacity compared to the literature without multiplication by the porosity in the code.

We can see in figure 2.9 that the curve fits perfectly with Batchelor's law. As we saw in chapter 1 with equation 1.7, the Krieger's law depends on the maximum compacity which can be used as a fit parameter. We have tested several parameters and have noticed that it is for a c_{max} of 0.62 that our results are the closest to the Krieger curve.

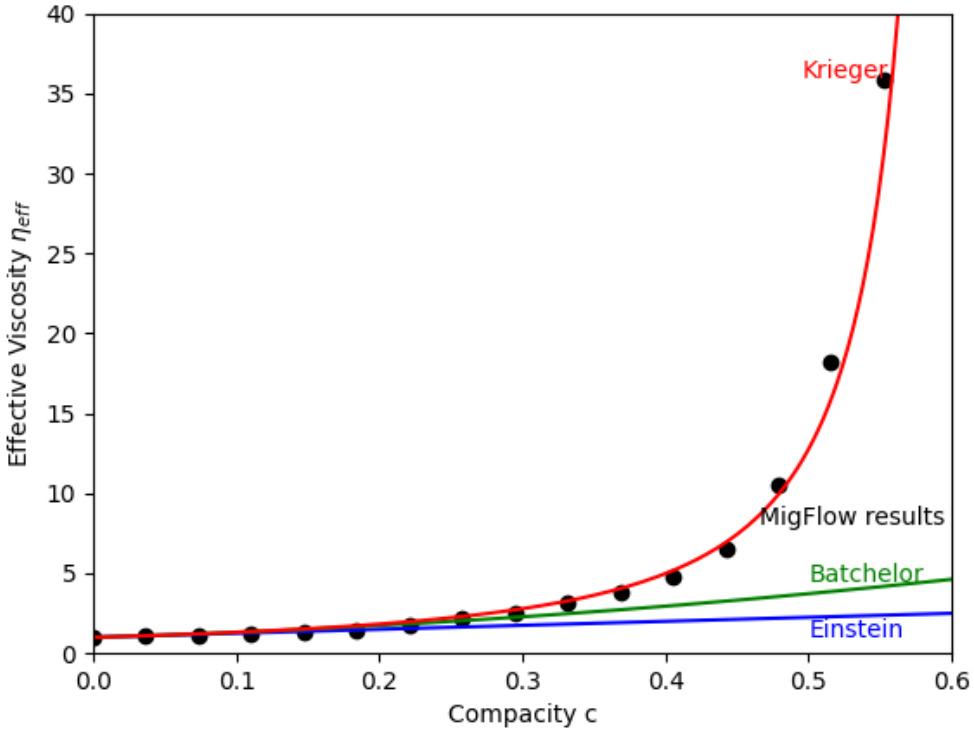

Figure 2.9: Viscosity in function of compacity compared to the literature with Batchelor's law inserted in the code.

Chapter 3

Parametric study

Now that we have a model that gives us the correct viscosity we can examine the influence of other parameters. We have already seen that if the compacity increases, the viscosity increases too. But there are other parameters that play a role in the viscosity of granular flow. We will discuss the effect of a change in the coefficient of friction between the grains on the value of the effective viscosity as well as on the values of the viscosities of the fluid and the grains separately. Next, we look at the normal forces acting on the upper boundary due to the grains. And finally, we act on the shear rate to observe shear thickening.

3.1 Friction coefficient

The coefficient of friction μ is an important parameter in the grain-grain interaction force. We will therefore perform the same simulation as in chapter 2 but for different friction coefficients in order to see its influence.

As it can be seen on figure 3.2, the higher the friction coefficient, the higher the viscosity. According to Coulomb law (equation 2.5) from section 2.1, the tangential force resulting from a contact between two grains depends on the normal force and the friction coefficient. Consider two grains that will collide such as figure 3.1. We can see the tangential and normal components of the resulting force. If our friction coefficient is high, the tangential force will be large. Therefore, the grain will undergo more rotation and less slip than for a smaller coefficient. This will cause a decrease in velocity and thus an increase in the viscosity.

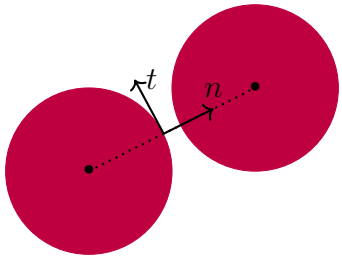

Figure 3.1: Two grains that will collide.

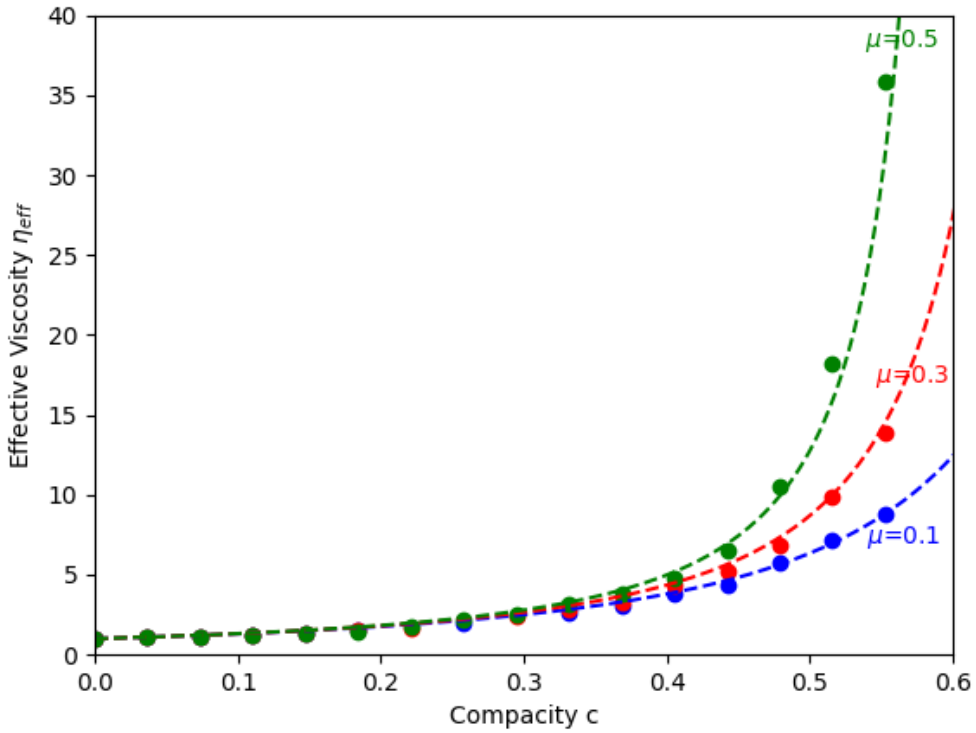

Figure 3.2: Viscosity in function of compacity compared to the Krieger curve with different coefficients of friction ($\mu = 0.1, 0.3, 0.5$ [-]).

As Krieger's law contains a fit parameter which is the maximum compacity, we have tested several values and found the ones that best fit our results. They are listed in table 3.1.

μ [-]	c_{max} [-]
0.1	0.88
0.3	0.71
0.5	0.62

Table 3.1: Krieger's fit parameter.

Then, we want to look at the influence of the friction coefficient on the fluid and on the grains separately.

We can see in figure 3.3 that the coefficient has almost no influence on the fluid, which is normal since it only contributes to the grain-grain interaction force. Regarding the influence on the particles, we can observe that at low compacities, the grains have no viscosity. This is due to the fact that the grains have very low probability to collide at low compacities. When the compacity increases, collisions start to occur and therefore the viscosity increases little by little and it increases more rapidly for a higher friction coefficient. If the coefficient is small, the viscosity of the fluid is more important than the one of the grains, therefore it is impossible for the granular flow to reach high viscosity values.

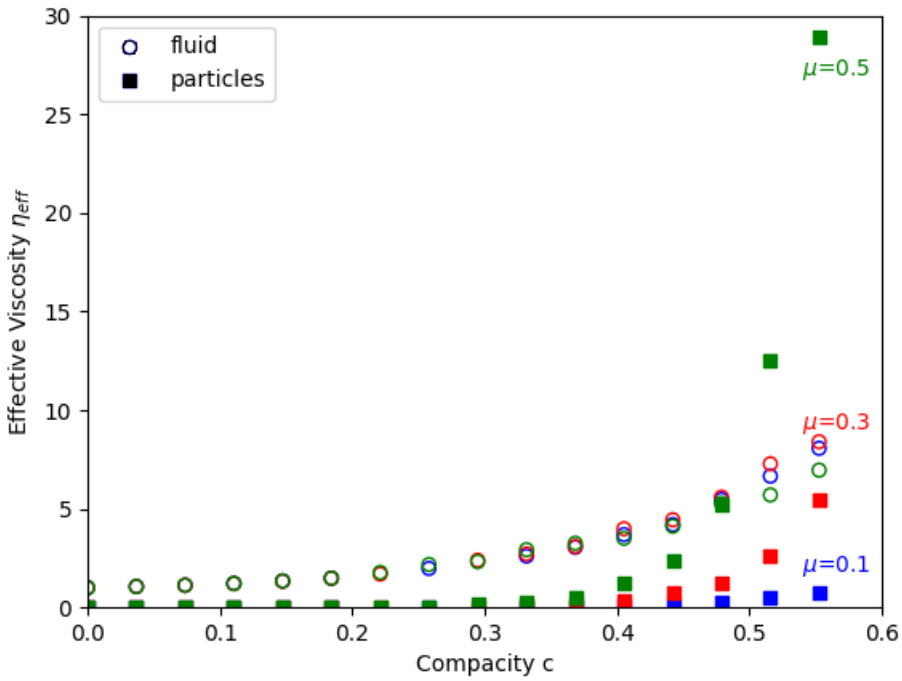

Figure 3.3: Fluid and grains viscosities in function of compacity with different coefficients of friction ($\mu = 0.1, 0.3, 0.5$ [-]). The fluid results are represented by an empty circle and the particles results are represented by a filled square.

3.2 Normal forces

We can look at the normal forces acting on the upper boundary for the case of the coefficient of friction of 0.5. In figure 3.4, it is the force applied by the grains that is displayed. We find the same behavior as in figure 3.3, that is to say that the more the compacity increases, the greater the force is. At the compacity of 0.2, we can see that the force is close to 0, that it increases slightly for a compacity of 0.4 and that it is much greater for the compacity of 0.5. We can also see that it takes a short time before the force reaches its average value. This is explained by the fact that the grains need time to start moving when they are sheared.

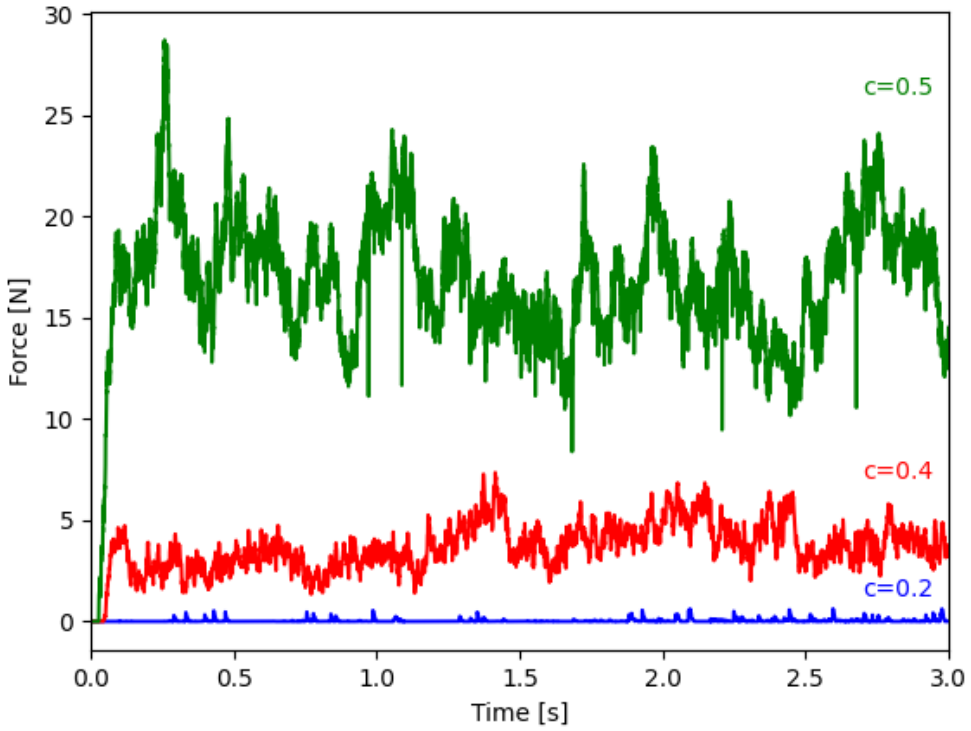

Figure 3.4: Normal force applied by the grain on the upper boundary for a coefficient of friction μ of 0.5 [-] and for different compacities (c= 0.2, 0.4, 0.5 [-]).

3.3 Shear thickening

In a Newtonian fluid, the viscosity does not change when the shear rate is changed. In suspensions, if the shear rate is increased, the viscosity rises. Therefore, compared to the Newtonian fluid for which the shear stress increases linearly with the shear rate, in suspensions, the shear stress increases more rapidly. This is because at low shear rates, the particles do not interact a lot with each other whereas at high shear rates, there is much more contact, resulting in an increase in shear stress. And the higher the shear rate, the more likely are the grains to collide with each other, so the shear increases even more.

In order to verify this behavior in our model, we are going to gradually change the shear rate $\dot{\gamma}$, thus the velocity of the top boundary. The simulation is done for shear rates ranging from 0.1 to 0.8 [m/s] and compacity of 0, 0.3 and 0.5. Both axis are scaled with respect to the maximum shear rate.

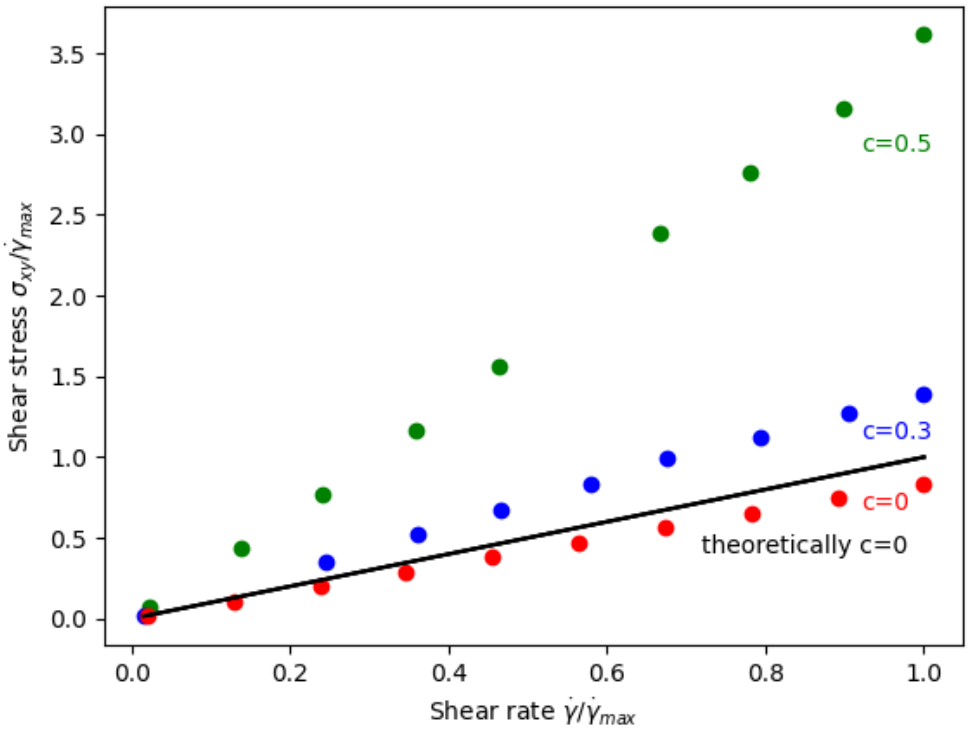

Figure 3.5: Shear stress as a function of the shear rate for different compacities (c = 0, 0.3, 0.5 [-]) and compared to the theoretical values. Axis are scaled with respect to the maximum shear rate.

It can be seen on figure 3.5 that for a compacity of 0, the values that the model returns are slightly smaller than the theoretical values. This is can be due to the fact that our model underestimates the values or to the fact that we do not do the simulations over a long enough time. Then for compacities of 0.3 and 0.5, we clearly observe shear thickening as expected. And the higher the compacity, the more shear thickening appears, which is consistent since the higher the compacity, the more collisions between grains are possible.

Afterwards, we kept the compacity at 0.3 but we changed the coefficient of friction between the grains.

As it can be seen in figure 3.6, increasing the friction indeed increases the shear stress. But it does not increase it a lot. Therefore, the compacity influences much more the shear stress than the friction coefficient between the grains as we have already seen in section 3.1.

What we can learn from this chapter is that increasing the coefficient of friction leads to an increase in viscosity and this only has an impact on the grains. It takes a little time for the grains to adapt to the shear and start moving. And increasing the shear rate increases the viscosity too.

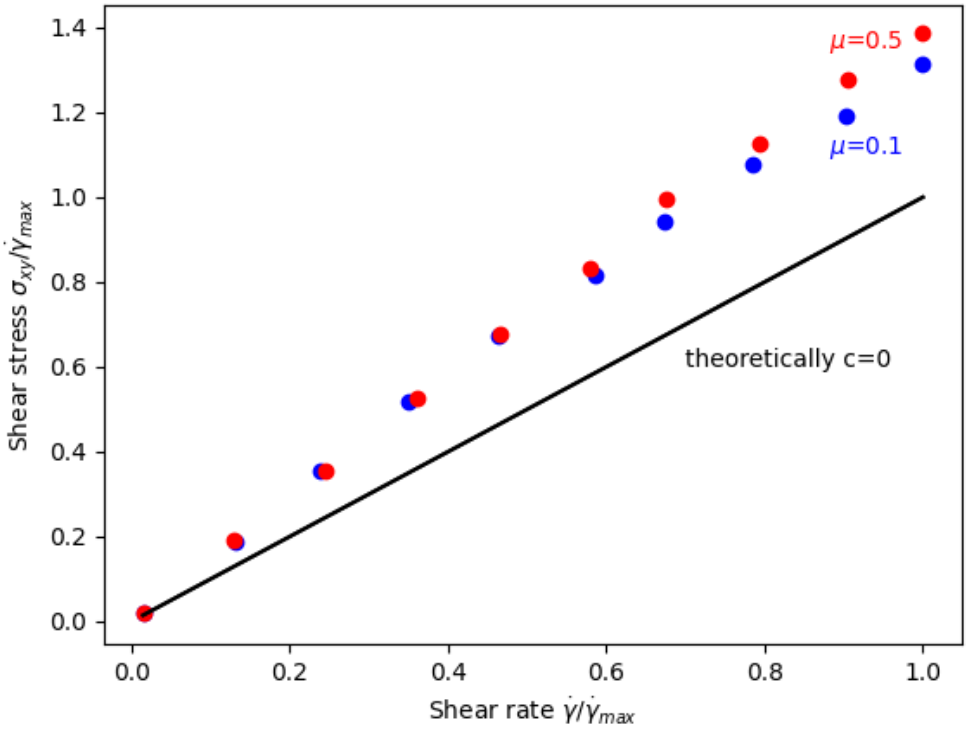

Figure 3.6: Shear stress as a function of the shear rate for different coefficients of friction ($\mu = 0.1, 0.5$) and for a compacity of 0.3 [-]. Axis are scaled with respect to the maximum shear rate.

Chapter 4

Frequential analysis

After studying the simple shear, we will look at a frequency analysis of the shear. For this, we perform a dynamic mechanical analysis. In this chapter, we will begin with the theory of this type of shear. Then we compare it with the results of *MigFlow* for which we present the parameters. We look at the case without grains first and then we add the grains and compare this with a one-dimension model. Lastly, we analyse the effect of the frequency on viscoelastic materials with the complex shear modulus.

To perform a dynamic mechanical analysis, an oscillating deformation is applied to a material and the stress response to this strain is analysed. Depending on the type of material, the response will have different behaviors. Let $\gamma(t)$ be the strain and $\sigma(t)$ be the stress. It can be seen in figure 4.1 that for an elastic solid, the stress is proportional to the strain and for a viscous liquid, the stress is $\pi/2$ out of phase with the strain.

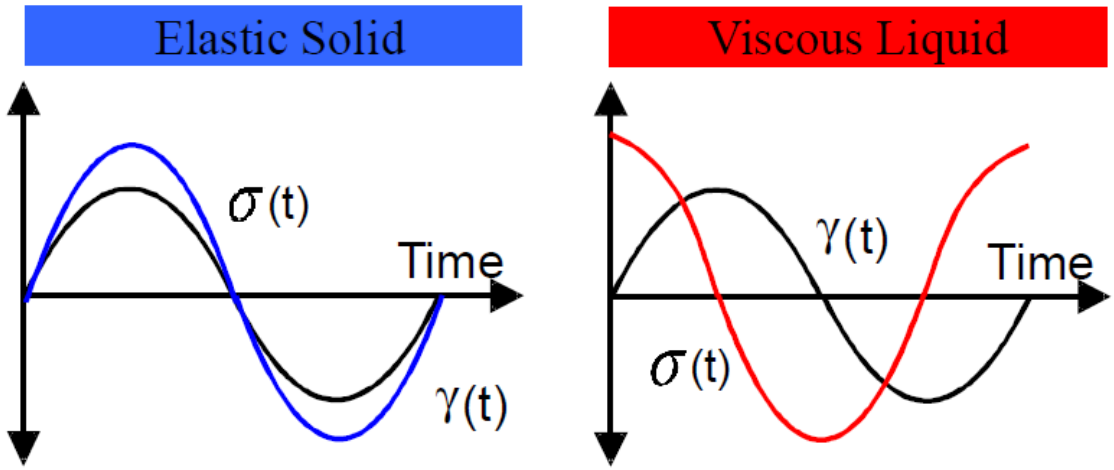

Figure 4.1: Theoretical stress response to strain for elastic solid (left) and for viscous liquid (right).

A viscoelastic material behaves both as a viscous liquid and as an elastic solid, therefore a combination of both idealized behaviors is represented in figure 4.2. Its phase angle δ is between 0 and $\pi/2$.

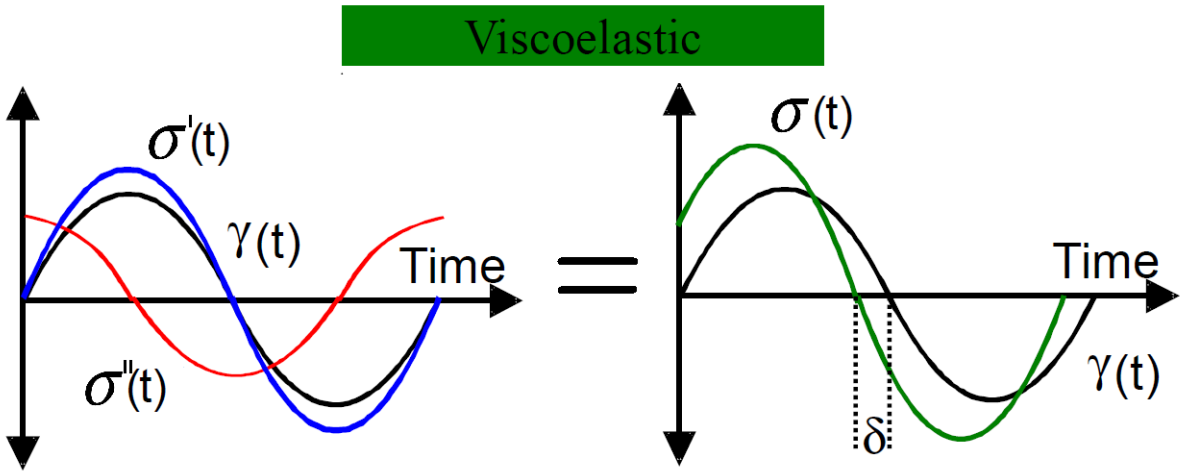

Figure 4.2: Theoretical stress response to strain for viscoelastic material.

The deformation is a sinusoidal function, so $\gamma(t) = \gamma_0 sin(\omega t)$. Therefore, the stress becomes $\sigma(t) = \sigma_0 sin(\omega t)$ for an elastic solid and $\sigma(t) = \sigma_0 \omega cos(\omega t)$ for a viscous liquid. For a viscoelastic component, it is the combination of both

$$\begin{aligned} \sigma(t) = \sigma_0 sin(\omega t + \delta) &= \sigma_0[cos(\delta)sin(\omega t) + sin(\delta)cos(\omega t)] \\ &= \gamma_0[G'(\omega)sin(\omega t) + G''(\omega)cos(\omega t)] \end{aligned} \tag{4.1}$$

with $G'(\omega)$, the storage or elastic modulus and $G''(\omega)$, the loss or viscous modulus which will be explained later.

4.1 Simulation

We are going to simulate an oscillating deformation with our model to see if it reacts as it should. The problem remains basically the same as for the simple shear. The main difference is the velocity of the top boundary. We force it to be a sinusoidal function as seen on table 4.1. The parameters that are different from the simple shear (Table 2.1) are listed in the table. We took a smaller domain in order to better realize the influence of the oscillating speed of the upper boundary on the whole domain.

Geometry:

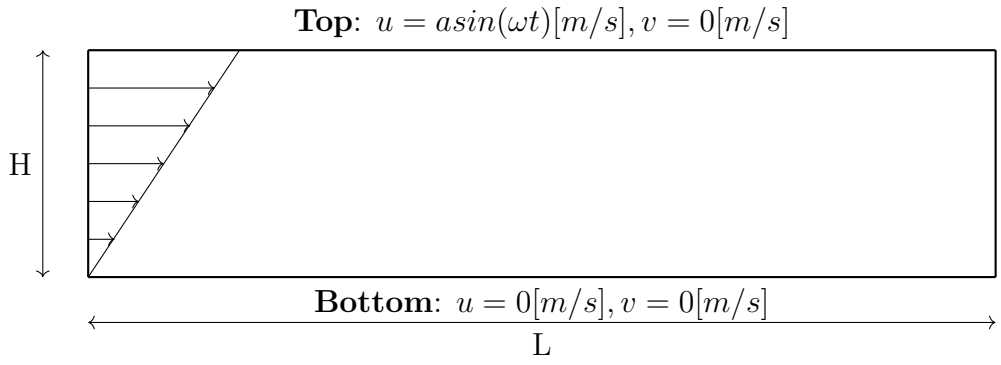

Parameters:

Domain height H = 0.001[m]	Frequency f = 1 [Hz]
Domain length L = 0.005 [m]	Angular frequency $\omega = 6.28[rad/s]$
Time step $\Delta t = 10^{-2}[s]$	Amplitude a = 0.1 [m]

Table 4.1: Illustration of the problem and boundary conditions.

4.1.1 Only fluid

First, we made the simulation without grains in order to verify the behavior of the viscous liquid.

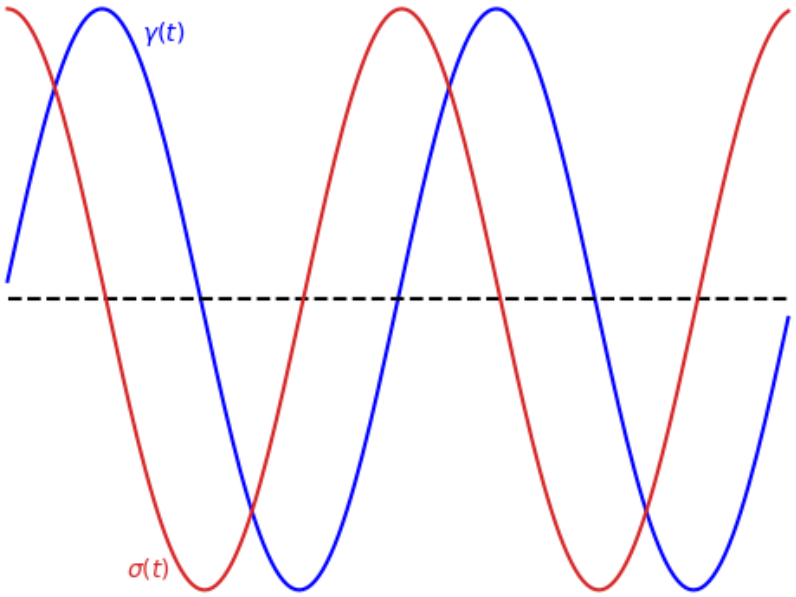

Figure 4.3: Stress response to strain for viscous liquid.

We can see in figure 4.3 that the response $\sigma(t)$ to the deformation $\gamma(t)$ is correct. Indeed, the stress is exactly $\pi/2$ out of phase with the strain. The two curves are put at the

same scale in order to observe correctly the phase shift, but there is normally a difference of amplitude between the two. As it is imposed, the amplitude of the strain is 0.1 and the resulting amplitude of the stress is 6.

4.1.2 Fluid and grains

Now that we have verified that the model was correct without the grains, we can add them to verify the behavior of the viscoelastic material. But first, we will modelise our problem in one-dimension in order to understand mathematically how we obtain the viscoelastic property. According to the theory, the response to a deformation for a viscoelastic material is a combination of a sine and a cosine. But we do not know exactly the proportion of both, so we will find the analytical expression with this one-dimension model.

We simplify the problem by studying a fluid with only one grain inside. The velocity of the fluid at the top boundary is still a sine function $u(t) = asin(wt)$.

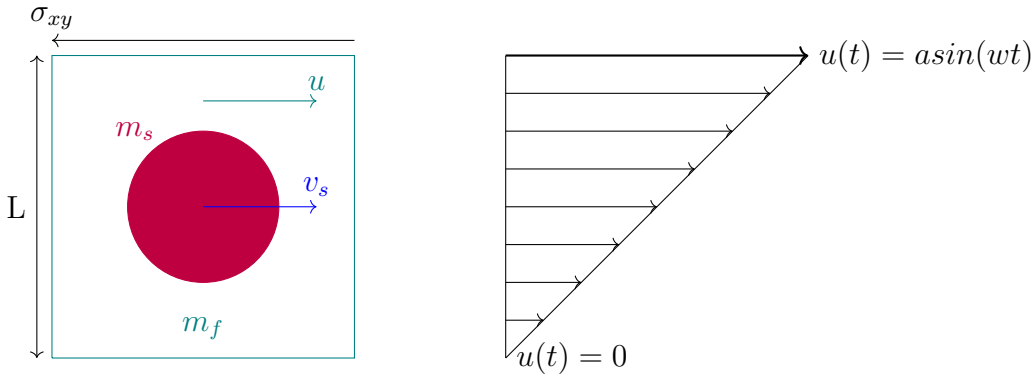

Figure 4.4: Illustration of the one-dimensional problem.

Figure 4.4 represents the problem. The grain has a velocity v_s, with a mass m_s and m_f is the mass of the fluid. σ_{xy} is the shear stress and L, the size of the domain.

We associate the problem to a damped mass-spring system. We use Newton's second law and the damping force definition: $F = kv$, with k the damping factor. Thus the equations resulting from this model are

$$\begin{cases} m_s \dfrac{dv_s}{dt}(t) = k(u(t) - v_s(t)) \\ m_f \dfrac{du}{dt}(t) = \dfrac{\sigma_{xy}}{L} + k(v_s(t) - u(t)) - \mu \dfrac{u(t)}{L^2} \end{cases} \tag{4.2}$$

with η is the dynamic viscosity of the fluid.

We solve the first equation which gives us:

$$v_s(t) = Ke^{\frac{-k}{m_s}t} - cos(wt)\frac{m_s wak}{k^2 + w^2 m_s^2} + sin(wt)\frac{ak^2}{k^2 + w^2 m_s^2} \tag{4.3}$$

Thanks to the initial condition $v_s(0) = v_{s0}$, we can find the value of the constant K:

$$K = v_{s0} + \frac{m_s wak}{k^2 + w^2 m_s^2} \tag{4.4}$$

And therefore,

$$v_s(t) = \left(v_{s0} + \frac{m_s wak}{k^2 + w^2 m_s^2}\right) e^{\frac{-k}{m_s}t} - cos(wt)\frac{m_s wak}{k^2 + w^2 m_s^2} + sin(wt)\frac{ak^2}{k^2 + w^2 m_s^2} \tag{4.5}$$

Finally, we can solve the second equation to find the shear σ_{xy}

$$\begin{aligned}
\sigma_{xy} &= m_f awL cos(wt) + \mu\frac{asin(wt)}{L} \\
&- kL\left[\left(v_{s0} + \frac{m_s wak}{k^2 + w^2 m_s^2}\right) e^{\frac{-k}{m_s}t} - cos(wt)\frac{m_s wak}{k^2 + w^2 m_s^2} + sin(wt)\frac{ak^2}{k^2 + w^2 m_s^2} - asin(wt)\right] \\
&= cos(wt)\left(m_f awL + kL\frac{m_s wak}{k^2 + w^2 m_s^2}\right) + sin(wt)\left(\mu\frac{a}{L} - kL\frac{ak^2}{k^2 + w^2 m_s^2} + kLa\right) \\
&- kL\left(v_{s0} + \frac{m_s wak}{k^2 + w^2 m_s^2}\right) e^{\frac{-k}{m_s}t}
\end{aligned} \tag{4.6}$$

We obtained the exact expression for the stress and therefore the proportions of sine and cosine. This allows us to obtain the expression of δ.

In order to illustrate these calculations, we have replaced the parameters by the values of our simulation with *MigFlow*, which are listed in table 4.1.2.

Parameters:	
Solid mass $m_s = 20$ [kg]	Frequency f = 1 [Hz]
Fluid mass $m_f = 50$ [kg]	Angular frequency $\omega = 6.28$[rad/s]
Damping factor k = 1 [Ns/m]	Amplitude a = 1 [m]
Size of domain L = 1 [m]	Dynamic viscosity $\mu = 1$ [Pas]

Table 4.2: Parameters of the one-dimensional problem.

We made the graph of the strain and the stress in figure 4.5. Again, the scale is the same but in reality the amplitude of the deformation is 0.1 and the one of the response is 0.97. The phase shift is of $4.8\pi/10$.

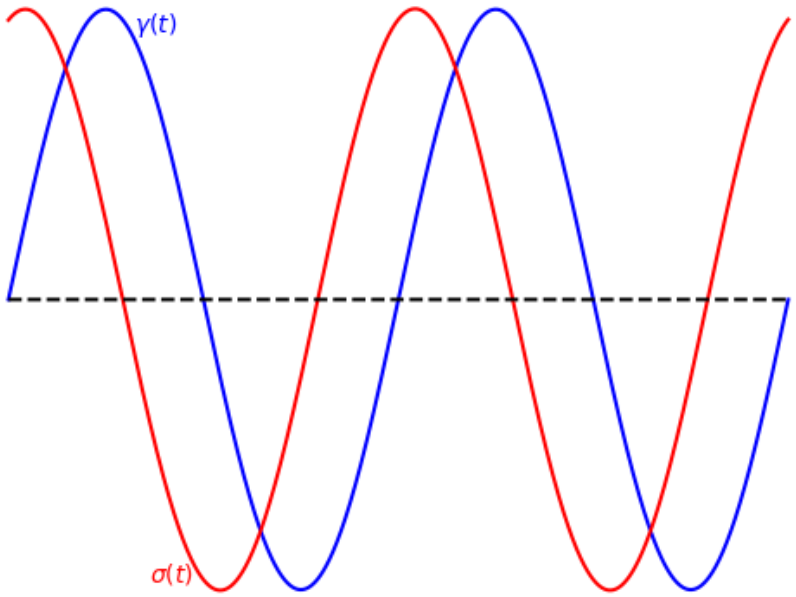

Figure 4.5: Stress response to strain for the one-dimensional problem.

The fact that the graph shows a phase shift allows us to justify that an under-resolved approach can work. Indeed, *MigFlow* tends to underestimate reality as it was already mentioned. There is no need to modelise everything in order to observe the right behavior.

Then, we made the simulation with grains on *MigFlow*. The parameters of the simulation are the same as for the simple shear (Table 2.1) except that the top boundary velocity is the sine function of the frequential analysis for the viscous liquid (Table 4.1). The results are shown in figure 4.6. The amplitude of the stress if of 0.1, as imposed and the one of the strain is between 60 and 65. The phase shift is of $6.8\pi/10$.

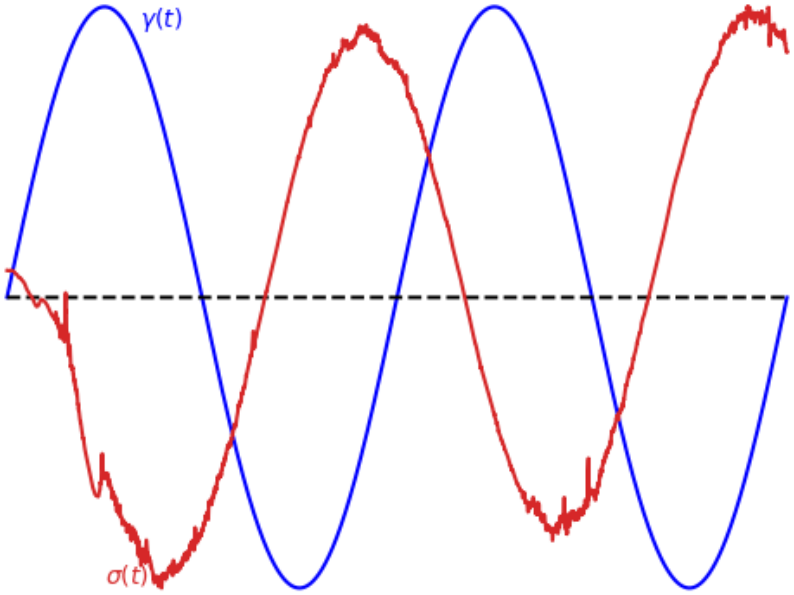

Figure 4.6: Stress response to strain for viscoelastic material.

The stress curve is not smooth, it shows small oscillations. This is due to the presence of grains. Indeed in the simulation of simple shear, we take the average stress over a period of 2 seconds with a very small time step. This makes the value very accurate since it is averaged over a large amount of data. However, in the case of frequencial shear, we cannot average the stress because the value of the upper boundary is constantly changing, so we can only obtain one value of stress each time.

The difference of phase shift between the one-dimension model and the *MigFlow* model can be explained by the fact that our one-dimension model is too simplistic. Indeed, since the solid phase is represented by a single large grain encompassing all the particles, there are many phenomena that are not taken into account. Like the collisions between the grains for example.

This can also be due to the fact that *MigFlow* has difficulty to account for frequential analysis. It takes a little time for the grains to adapt to a velocity as we have already seen, so here since the velocity is constantly changing, they may not have time to adapt properly and therefore the phase shift may not be correct. Indeed, the phase shift is bigger than $\pi/2$. This can also come from the fact that the fluid and solid phases are resolved separately and the coupling between both is therefore weak.

But what has to be remembered is that in both cases, the appearance of the graph is correct i.e. there is a phase shift.

4.2 Complex shear modulus

Viscoelastic materials are characterized by the frequency at which they are sheared. The complex shear modulus is defined

$$G^*(\omega) = G'(\omega) + iG''(\omega) \tag{4.7}$$

Its real part $G'(\omega)$ is the storage modulus which represents the amount of energy stored elastically in one cycle of the angular frequency. Its imaginary part $G''(\omega)$ is the loss modulus which is the quantity of energy dissipated viscously during one cycle too. We can define δ thanks to these moduli as it can be seen in figure 4.7.

$$tan(\delta) = \frac{G'(\omega)}{G''(\omega)} \tag{4.8}$$

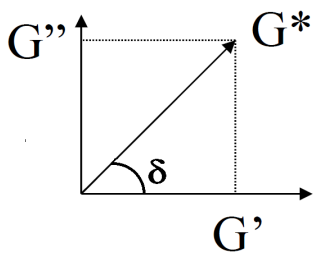

Figure 4.7: Complex diagram of the shear modulus.

Fernanda et al. [26] have studied the behavior of the two moduli and we can see their results in figure 4.8. At both high and low frequencies, the storage modulus has a constant value. Whereas at frequencies inbetween, it rises until it reaches its plateau value. The loss modulus is very small at low frequencies, then it rises until it reaches and peak and right after it falls back down to a plateau value.

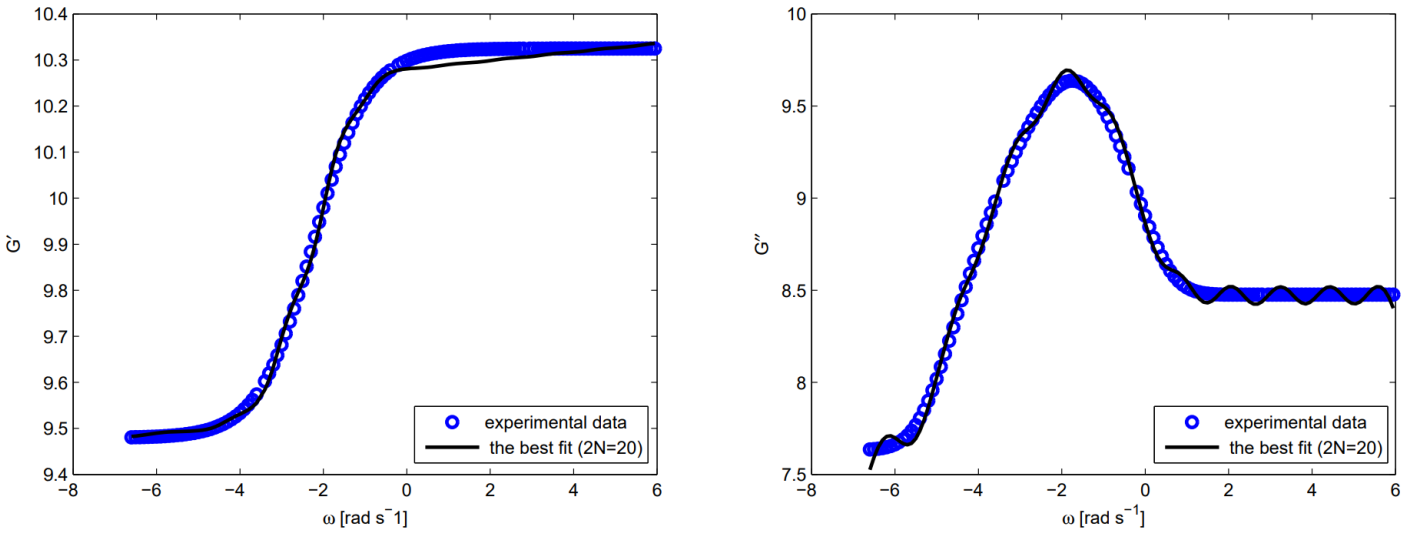

Figure 4.8: Storage modulus (left) and loss modulus (right) as function of the frequency obtained by Fernanda et al. [26].

We made the simulation in *MigFlow* to obtain the moduli of our model. The simulation is the same as before but this time the frequencies are going from 1 [Hz] to 10 [MHz]. The results are shown in figure 4.9.

We observe the same behavior as in figure 4.8 especially for the storage modulus. Indeed, it also starts with a plateau value and then increases very strongly before reaching another plateau value. On the other hand, the loss storage shows a little difference. Indeed, it also shows a steep rise to reach a peak value and then it falls back down to a plateau value. But in our simulation, this plateau value is smaller than the value for small frequencies, unlike the simulation of Fernanda et al. for which the value is higher. This is probably due to the fact that we did not made the simulation for even smaller frequencies.

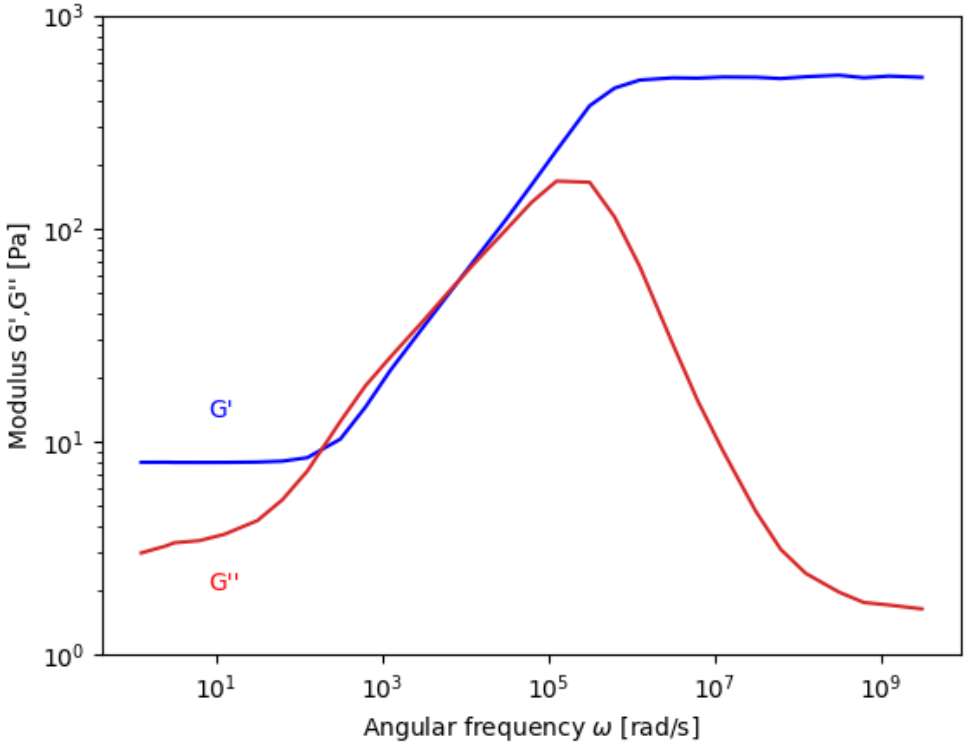

Figure 4.9: Storage modulus and loss modulus in function of the frequency.

This can be explained mathematically. Indeed, in 2001, Roylance [27] studied linear viscoelasticity in order to understand better how to analyze this kind of material. For him, the viscoelastic response to the frequency is analogous to the time dependance of reactive electrical circuits. He defined the Maxwell model with a Hookean spring and a Newtonian dashpot which can be seen on illustration 4.10 with k, the spring constant which is expressed in $[N/m^2]$.

Figure 4.10: Maxwell model with Hookean spring (left) and Newtonian dashpot (right).

Defining τ as the ratio of viscosity to stiffness $\tau = \eta/k$, he defines the constitutive equation for the Maxwell material

$$k\dot{\gamma} = \dot{\sigma} + \frac{1}{\tau}\sigma \tag{4.9}$$

In the case of a dynamic response, the time dependencies for the strain and the stress are an exponential $e^{i\omega t}$. Therefore, equation 4.9 becomes

$$k(i\omega)\gamma_0 e^{i\omega t} = (i\omega + \frac{1}{\tau})\sigma_0 e^{i\omega t} \tag{4.10}$$

Then, we assume the real part of $G^*(\omega)$ to be completely in phase with the strain and its imaginary part to be $\pi/2$ out of phase with it and thanks to equation 4.1, we can rewrite $G'(\omega)$ and $G''(\omega)$ and inject them inside equation 4.7, so $G^*(\omega)$ becomes

$$G^*(\omega) = \frac{\sigma_0}{\gamma_0} \tag{4.11}$$

And with equation 4.10, we obtain

$$G^*(\omega) = \frac{k(i\omega\tau)}{1 + i\omega\tau} = \frac{k\omega^2\tau^2}{1 + \omega^2\tau^2} + i\frac{k\omega\tau}{1 + \omega^2\tau^2} \tag{4.12}$$

In equation 4.12, the storage modulus and loss modulus are explicitly given as they are the real and imaginary part of $G^*(\omega)$.

Therefore, if we take $\tau\omega$ as a dimensional frequency, we can quickly understand the behavior of the moduli. Indeed, for the storage modulus, for very small values of $\tau\omega$, the term $\omega^2\tau^2/(1 + \omega^2\tau^2)$ tends to 0 so on a logarithmic scale, it gives a small plateau value. Then the term becomes bigger and bigger until it reaches a plateau value again when the term tends to 1. For the loss modulus, the term $\omega\tau/(1 + \omega^2\tau^2)$ is close to 0 for small values of $\tau\omega$ then it becomes larger but for large values of $\tau\omega$ it decays until it reaches values near 0 again.

Therefore, we think that normally the loss storage should reach a plateau value for large values of $\tau\omega$ but that this value must be much smaller than the one of Fernanda et al., it should be equal to its value for very small $\tau\omega$. Moreover, the orders pf magnitude of the frequencies are not at all the same. This is due to the fact that we do not have the same parameters as in the article.

We can therefore conclude that the *MigFlow* model is more or less able to account for a frequency analysis. Indeed, the values are not the same but the behavior is correct.

Conclusion

The aim of this thesis was to perform an investigation of the viscoelastic properties of suspensions and to verify that the *MigFlow* model corresponds correctly to the reality.

In the first chapter, a state of the art of the viscosity was presented. First, the different instruments to measure viscosity were described. Then it was seen that to measure the viscosity of a fluid it is easier to measure it in relation with the viscosity of a known fluid. Water was chosen as a reference and therefore the different experiments to calculate its value were presented. Afterwards, the different models to calculate the viscosity of a granular flow were presented. Finally, the approach to obtain the equations of motion of a suspension was explained.

In the second chapter, we performed the simulation of a simple shear in order to study the resulting viscosity. To realize this simulation, we used the software *MigFlow* and we explained the method it uses to solve the fluid and grains equations. We then described the problem with its boundary condition. The mesh is created with the GMSH software and we explained how the generation of the grains is done. Afterwards, we validated the model. The porosity and the fluid velocity being accurate, we focused on the viscosity versus compacity curve and compare it with the literature models. We realized that *MigFlow* did not calculate the viscosity correctly. Indeed, the viscosity was evaluated below 1 for low compacities, which is physically impossible. We therefore made the correction in the code in order to obtain results corresponding properly to the literature. We saw that the viscosity is increasing with the compacity.

In chapter 3, we performed a parametric study. First, we looked at the influence of the friction coefficient. We observed that increasing the coefficient strongly increased the viscosity for high compacities. We therefore looked at the viscosity of the fluid and the grains separately in order to better understand this behavior. We noticed that the coefficient did not influence the behavior of the fluid. Such a comportment is normal, since the coefficient does not appear in the equation that describes the fluid. Concerning the grains, their viscosity is zero at low compacities. This is due to the fact that their chance of colliding are very small. The more the compacity increases, the more the collisions between the grains become numerous. And the more the coefficient increases, the stronger these collisions are and the viscosity is therefore greater. Second, we looked at the normal force applied by the grains on the upper boundary of the domain. What we notice is that it takes a small time period before the grains start to react to the shear. Finally, we studied the influence of the shear rate. We notice that at zero compacity, our stress did not increase quite linearly as a Newtonian fluid is supposed to do. This is because our model slighlty underestimates the viscosity. But otherwise, we do observe

some shear thickening that becomes more and more important as the shear rate increases. And this increase is even stronger in the case of higher compacities.

In the final chapter, we performed a frequency analysis. The velocity on the upper boundary is a sinusoidal function and we study the stress response to this deformation. We first review the theory. For an elastic solid, the stress and the strain are in phase, for a purely viscous fluid they are $\pi/2$ out of phase. For a viscoelastic material, it is a combination of both. We perform the simulation on *MigFlow* and we obtain the perfect behavior in the case without grains. For the case with grains, we first present a one-dimensional model to prove that an under solved approach can give a correct behavior since *MigFlow* underestimates a little the values. Then we compare the one-dimensional simulation with the *MigFlow* simulation. There is a phase difference between the two which can be due to the fact that the one-dimensional model is too simplistic. It can also be due to the fact that since it takes a small time for the grains to react to a shear and that here the shear is not constant, the grains do not have time to adapt properly. Or it can be due because the liquid and solid phases are resolved separately and therefore the coupling between the two is weak. Moreover, we observe oscillations on the response of the *MigFlow* model. This is due to the fact that in normal shear the stress is calculated by a time average and that here, since we are in a frequency shear, it is not possible to perform a time average. Then we study the complex shear modulus. These are the loss and conservation moduli which represent the amount of energy dissipated and conserved by the material. We prove mathematically the shape of the curves thanks to the Maxwell model. We find that the storage modulus must be a plateau value at low frequencies, which then rises to reach a higher plateau value at high frequencies. For the loss modulus, it starts at very small values, then rises to a peak to fall back to a very small plateau value.

We were able to solve the problem of the viscosity which did not correspond to the curves of the literature. We made some modifications in the code and it is now assumed to be correct. Some errors remain in the model, which means that the reality of the physical phenomena could not be perfectly reached. However, the shapes of the different curves are close to reality in general which is promising for the project *MigFlow*.

Bibliography

[1] D. Pinho, V. Carvalho, I. M. Gonçalves, S. Teixeira and R. Lima, "Visualization and Measurements of Blood Cells Flowing in Microfluidic Systems and Blood Rheology: A Personalized Medicine Perspective," *Journal of Personalized Medicine*, 2014. DOI: 10.3390/jpm10040249.

[2] M. Pastor, T. Blanc, B. Hadda, V. Drempetic, M. Sanchez Morles, P. Dutto, M. Martin Stickle, P. Mira and J. Fernandez Merodo, "Depth average models for fast landslide propagation: Mathematical, rheological and numerical aspects," 2020. DOI: 10.1007/s11831-014-9110-3.

[3] P. Fischer and E. Windhab, "Rheology of food materials," *Elsevier*, 2010. DOI: 10.1016/j.cocis.2010.07.003.

[4] A. Perrot, D. Rangeard, S. Amziane and M. Sonebi, "Défis à relever en termes de rhéologie des matérieux cimentaires pour une impression 3D par extrusion/dépôt," *Academic journal of civil engineering*, 2019. DOI: 10.26168/ajce.36.1.43.

[5] J. Goodwin and R. Hugues, "Rheology for chemists: An introduction," in *Royal Society of Chemistry*. 2008. DOI: 10.1515/arh-2006-0030.

[6] R. P. Chhabra, "Non-newtonian fluids: An introduction," in *Rheology of Complex Fluids*. Springer New York, 2010, pp. 3–34. DOI: 10.1007/978-1-4419-6494-6_1.

[7] M. Constant, F. Dubois, J. Lambrechts and V. Legat, "Implementation of an unresolved stabilised FEM-DEM model to solve immersed granular flows," *Computational Particle Mechanics*, 2018. DOI: 10.1007/s40571-018-0209-4.

[8] R. Williams, "Determination of viscometric data from the Brookfield R.V.T. viscometer," *Department of Applied Mathematics, University College of Wales, Aberystwyth*, 1979. DOI: 10.1007/BF015158280.

[9] S. Koch, T. Schneider and W. Küter, "The velocity field of dilute cationic surfactant solutions in a Couette-viscometer," *Universität Dortmund*, 1997. DOI: 10.1016/S0377-0257(98)00058-5.

[10] J. Kestin, M. Sokolov and W. Wakeham, "Theory of capillary viscometers," *Brown University*, 1973. DOI: 10.1007/BF00382489.

[11] S. Gupta, "Viscometry for liquids," in Springer, 2014, vol. 194, ch. 5: Oscillating viscometers.

[12] J. Kelley, T. Roberts and H. Harris, "A penetrometer for measuring the absolute viscosity of glass," *U.S.Dept. of the Interior, Bureau of Mines*, 1964.

[13] J. Swindells, J. Coe and T. Godfrey, "Absolute viscosity of water at 20 C," *Journal of Research of the National Bureau of Standards*, 1952.

[14] R. Roscoe and W. Bainbridge, "Viscosity Determination by the Oscillating Vessel Method II: The Viscosity of Water at 20C," *Physics Department, King's college, Newcastle upopn Tyne*, 1958. DOI: 10.1088/0370-1328/72/4/313.

[15] J. Kestin and J. Shankland, "The Free Disk as an Absolute Viscometer and the Viscosity of Water in the Range 25-150 C," *Division of engineering, Brown University*, 1981. DOI: 10.1515/jnet.1981.6.4.241.

[16] D. Berstad, B. Knapstad, M. Lamvik, P. Skjølsvik, K. Tørklep and H. Øye, "Accurate measurements of the viscosity of water in the temperature range 19.5-25.5 C," *Institutt for Uorganisk Kjemi*, 1987. DOI: 10.1016/0378-4371(88)90015-5.

[17] The International Association for the Properties of Water and Steam, "Release on the IAPWS Formulation 2008 for the Viscosity of Ordinary Water Substance," 2008. Available at: http://www.iapws.org.

[18] ——, "Revised Supplementary Release on Properties of Liquid Water at 0.1MPa," 2011. Available at: http://www.iapws.org.

[19] A. Einstein, "A new determination of the molecular dimensions," *Annalen der Physik 19, 289-306*, 1906.

[20] ——, "Correction of my work : A new determination of the molecular dimensions," *Annalen der Physik 34, 591-592*, 1911.

[21] G. Batchelor, "The effect of Brownian motion on the bulk stress in a suspension of spherical particles," *Journal of Fluid Mechanics*, 1977.

[22] I. Krieger and T. Dougherty, "A Mechanism for Non-Newtonian Flow in Suspensions of Rigid Spheres," *The Society of Rheology*, 1959. DOI: 10.1122/1.548848.

[23] T. Anderson and R. Jackson, "A fluid mechanical description of fluidized beds," *University of Edinburgh, Scotland*, 1967. DOI: 10.1021/i160024a007.

[24] A. Robert, *IGERT:SPH and Free Surface Flow*, https://www.slideserve.com/gloria/igert-sph-and-free-surface-flows, [Online; accessed 10/08/22], 2001.

[25] C. Geuzaine and J.-F. Remacle, "Gmsh : A 3-D finite element mesh generator with built-in pre- and post-precessing facilities," *International journal for numerical methods in engineering 79, 1309-1331*, 2009. DOI: 10.1002/nme.2579.

[26] M. Fernanda, P. Costa and C. Ribeiro, "Parameter estimation of viscoelastic materials: A test case with different optimization strategies," *Dept. of Mathematics and Applications, University of Minho, Portugal*, 2011. DOI: 10.1063/1.3636846.

[27] D. Roylance, "Engineering viscoelasticity," *Department of Materials Science and Engineering, Massachusetts Institute of Techonoly, Cambridge*, 2001.

UNIVERSITÉ CATHOLIQUE DE LOUVAIN
École polytechnique de Louvain
Rue Archimède, 1 bte L6.11.01, 1348 Louvain-la-Neuve, Belgique | **www.uclouvain.be/epl**